

# More ATP Does Not Equal More Contractility: Power And Remodelling In Reconstituted Actomyosin

Sami C. Al-Izzi,<sup>1,\*</sup> Darius V. Köster,<sup>2,†</sup> and Richard G. Morris<sup>1,‡</sup>

<sup>1</sup>*School of Physics and EMBL Australia Node in Single Molecule Science,  
School of Medical Sciences, University of New South Wales - Sydney 2052, Australia*

<sup>2</sup>*Centre for Mechanochemical Cell Biology and Division of Biomedical Sciences,  
Warwick Medical School, University of Warwick, Coventry CV4 7AL, United Kingdom*

The cytoskeletal component actomyosin is a canonical example of active matter since the powerstroke cycle locally converts chemical energy in the form of adenosine triphosphate (ATP) into mechanical work for remodelling. Observing myosin II minifilaments as they remodel actin *in vitro*, we now report that, at high concentrations of ATP, myosin minifilaments form meta-stable swirling patterns that are characterised by recurrent vortex- and spiral-like motifs, whereas at low concentrations of ATP, such structures give way to aster-like patterns. This is shown to be consistent with the (quasi-)steady states of a polar active hydrodynamic theory of actomyosin whose ATP-scaling is obtained from a microscopic description for the ATP-dependent binding statistics of the headgroups of single myosin II minifilaments. The latter codifies the heuristic that, since the powerstroke cycle involves the unbinding of myosin II headgroups from actin, increases in the concentration of ATP reduce the likelihood that a given myosin II minifilament has more than one headgroup bound simultaneously, reducing its ability to generate contractile forces and increasing the relative likelihood of processive motion. As a result, our work demonstrates how ATP not only controls the rate at which work is done— *i.e.*, the power— but also the mode by which this occurs.

## I. INTRODUCTION

Actomyosin—the cortical meshwork of actin filaments and myosin II motors—is a cytoskeletal component that is crucial for many cellular functions, including morphogenesis, motility and division [1–3]. It is also a central example of active matter [4], since the ATPase activity of myosin II head-groups couples the hydrolysis of bound Adenosine Triphosphate (ATP) with a conformational change, locally converting chemical energy into mechanical forces via the so-called powerstroke cycle [5].

However, whilst the rate at which work can be done by actomyosin is ultimately set by the balance between ATP and its hydrolysis products, Adenosine Diphosphate (ADP) and Phosphate (Pi), evidence from several *in vitro* studies increasingly suggests that the relationship between the concentration of available ATP and the behaviour of actomyosin is complex: ATP has variously been shown to influence actin meshwork pattern formation [6], rheology [7], actin filament breaking [8], and myosin II processivity [9].

To better understand the relationship between remodelling and power, we combine total internal reflection fluorescence (TIRF) microscopy and interferometric scattering (iSCAT) microscopy [10, 11] to observe actomyosin reconstituted on supported lipid bilayers (SLBs). TIRF is used to image remodelling of the actin architecture, whilst iSCAT—a label-free approach that relies on the interference between reflected and scattered

light from nano-objects near an interface—is used to observe myosin II minifilaments (oligomers of up to  $\sim 50$  individual myosin II molecules) over long times without the deterioration and/or inactivation of myosin due to photodamage. Notably, at intermediate-to-high concentrations of ATP, we report recurrent meta-stable actomyosin structures, such as vortex- and spiral-like motifs, where myosin II minifilaments travel along actin filaments. Such swirling and dynamic structures are in contrast with the aster-like patterns formed as the available supply of ATP depletes.

We compare these dynamic and emergent patterns with the (quasi-)steady states of a polar active hydrodynamic description of our *in vitro* system. However, since ATP is depleted over the lifetime of our assays, it is not a hydrodynamic quantity. Therefore, we must use a microscopic, stochastic model for the bound status of the headgroups of a single myosin II minifilament in order to derive an ATP-scaling ansatz for the active coefficients in our hydrodynamic theory. This encodes the fact that, since the powerstroke cycle involves the unbinding of myosin II headgroups from actin, increases in the concentration of ATP reduce the likelihood that a given myosin II minifilament has more than one headgroup bound simultaneously, reducing its ability to generate contractile forces as well as increasing the relative likelihood of processive motion. The result is that the nascent contractile instability—where force generating myosins are advected by the contractile remodelling that they themselves induce—only occurs beneath a threshold of ATP.

Our work is therefore an example of how critical biochemistry can be included in symmetry-based hydrodynamic descriptions in order to reproduce important biological function. In this case, we see that the dependence

\* s.al-izzi@unsw.edu.au

† d.koester@warwick.ac.uk

‡ r.g.morris@unsw.edu.au

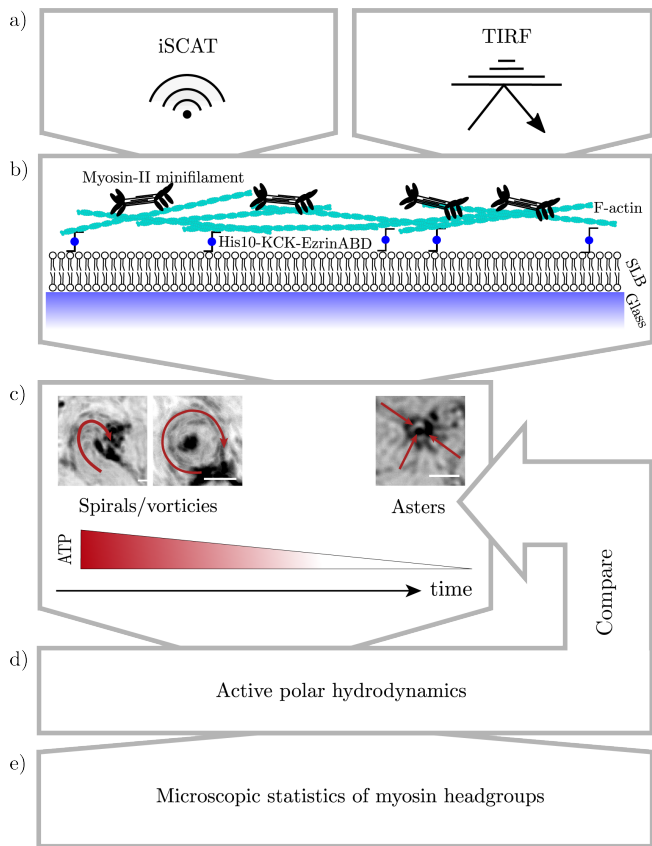


FIG. 1. **Schematic outline of paper.** Interferometric scattering (iSCAT) and total internal reflection fluorescence (TIRF) microscopy (a) are used to observe actomyosin reconstituted *in vitro* on a supported lipid bilayers (SLB) (b). At high concentrations of ATP, myosin minifilaments form metastable swirling patterns that are characterised by recurrent vortex- and spiral-like motifs, whereas as ATP depletes, such structures give way to aster-like patterns (c). We show that such patterns are captured by a polar active hydrodynamic theory (d) whose active coefficients take a functional form obtained from a microscopic, statistical model of the ATP-dependent headgroup kinetics of a single myosin II minifilament (e).

of actomyosin remodelling on ATP relates to the precise nature of the powerstroke cycle as well as the multivalent structure of myosin II minifilaments, resulting in a novel and non-trivial relationship between power and remodelling.

## II. ASTERS, SPIRALS AND VORTICES REVISITED

We start with actomyosin reconstituted *in vitro* on supported lipid bilayers [12–18]: a system previously shown to readily remodel under the action of ATP, forming asters and contractile foci under a variety of conditions [14, 15]. Specifically, we follow [9] and use iSCAT microscopy to observe the motion of myosin II minifil-

aments atop a texture of intermediate length F-actin ( $l_{\text{actin}} = 9 \pm 5.5 / 7 \pm 4.7 / 6 \pm 4.6 \mu\text{m}$ ), itself attached to fluid lipid-bilayer supported by a glass substrate (Fig. 2a). Our central observation is that, whilst aster-like contractile foci can be observed once ATP has been depleted (Vid. 1), at earlier times, when concentrations of ATP are estimated to be around  $1\text{--}10 \mu\text{M}$  [6, 8] we also observe complex swirling patterns. These are characterised by recurrent dynamical vortex- and spiral-like motifs, where myosin II minifilaments tightly circle either a void or a myosin II rich centre (Fig. 2d, Vid. 2-5, SM Sec. 2 [19]). On rare occasions, we also see such structures merge to form a larger foci (Vid. 6). The average diameter of the circular motion was  $4.5 \pm 1.3 \mu\text{m}$ , with particle image velocimetry (PIV) [20–22] characterising peak speeds on the order of  $100 \text{ nm s}^{-1}$  (see SM Sec. 2 [19]). The lifetimes of the motifs all exceeded 90 s, which is far greater than the average residence time of individual minifilaments [9], and indicative of a quasi-stable state whereby the incoming and outgoing fluxes of minifilaments are almost balanced.

Since the iSCAT signal of actin filaments is very low in comparison to the myosin signal, we separately observed fluorescently labelled actin filaments under similar conditions using total internal reflection fluorescence (TIRF) microscopy (Fig. 2c and SM Sec. 1 [19]). Again, this revealed long-lived vortex-like motion (Fig. 2e, Vid. 7-8, SM Sec. 2), with circular motifs of average diameter  $3.7 \pm 1.5 \mu\text{m}$  and lifetimes  $> 100 \text{ s}$ . Strikingly, however, PIV revealed that speeds were  $1 - 5 \text{ nm s}^{-1}$ , significantly slower than those of the myosin II minifilaments (see SM Sec. 2 [19]). Moreover, the actin and myosin vortices flow in the same direction, and almost all the vortices are of the same handedness (29 out of 34). This latter feature we attribute to the chirality of actin inducing a twist-bend coupling [23–25], although a detailed investigation is considered out of scope for this article.

Nominally, such observations bare superficial similarities to the steady-state *asters*, *spirals* and *vortices* reported in a generic treatment of incompressible active polar gels [26]. However, the underlying physics of [26] differs considerably from that of our system, where myosin features explicitly, layered atop actin, and where both actin and myosin are compressible. The layering, or stratification of myosin and actin has been suggested to be an important organising factor elsewhere [27]. Moreover, there is a lack of evidence for either noticeable differences between the elastic moduli for splay and bend, or any noticeable active spontaneous-splay stresses, which drive the rotation of spirals in [26]. As a result, the only stable steady-states in our system should, in principle, be aster-like, which is in-line with the actin textures that we observe on depletion of ATP (and their behaviour on ATP add-back).

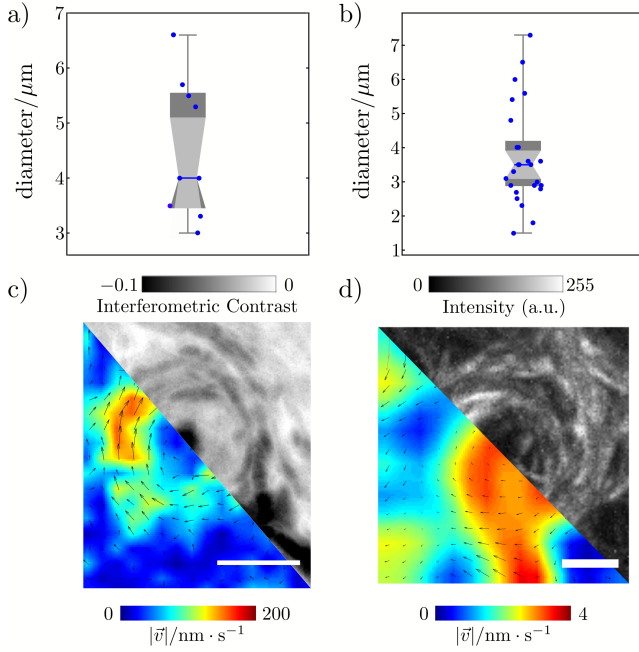


FIG. 2. **Meta-stable vortices and spirals at intermediate-to-high concentrations of ATP.** **a)** Approximately 10 min after addition of 0.1 mM ATP, networks with intermediate length F-actin ( $l_{\text{actin}} = 8 \pm 4.7 \mu\text{m}$  [28]) and an approximate minifilament-to-actin filament ratio of 3:1 displayed meta-stable spiral-like structures in iSCAT with an average diameter of  $4.5 \pm 1.3 \mu\text{m}$ . **b)** Observing a range of lengths ( $l_{\text{actin}} = 9 \pm 5.5 / 7 \pm 4.7 / 6 \pm 4.6 \mu\text{m}$ ) of fluorescently-labelled actin via TIRF at an approximate minifilament-to-actin ratio of 1:1 resulted in motifs with an average diameter  $3.7 \pm 1.5 \mu\text{m}$ . **c)** Representative minimal intensity projections (duration 120s, scale bar  $2\mu\text{m}$ ) and corresponding flow fields inferred using PIV analysis for iSCAT. **d)** Representative vortex TIRF maximal intensity projection (duration 120s, scale bar  $2\mu\text{m}$ ) with corresponding PIV analysis. (See SM [19] for more details).

### III. ACTIVE HYDRODYNAMICS OF *IN VITRO* ACTOMYOSIN

In order to explore the phenomenology that underpins our observations, we write down a nemato-hydrodynamic description of our *in vitro* system (SM Sec. 4 [19] & [4, 26, 29–32]). Whilst this overlooks some non-trivial aspects of the rheology of transiently-bound intermediate-length actin filaments (discussed later) we argue that such a symmetry-based approach is sufficient if we restrict ourselves to long-lived steady-state and quasi-steady-state behaviours only.

Since the depletion of bulk ATP is slow compared to its characteristic rate of diffusion, we adopt a quasi-static approach to ATP concentration. There are therefore only two continuity equations, one each for the density of myosin II minifilaments,  $\rho_m$ , and the density of actin filaments,  $\rho_a$ . Using myosin II minifilament residence time and run length as characteristic spatio-temporal scales

(SM Sec. 4 [19]) these take the dimensionless form

$$\partial_t \rho_m + \nabla_i J_m^i = \frac{\rho_a}{\rho_a + \rho_a^h} - k \rho_m, \quad (1)$$

and

$$\partial_t \rho_a + \nabla_i J_a^i = 0, \quad (2)$$

where  $J_m^i = \rho_m v_m^i$  and  $J_a^i = \rho_a v_a^i$  are the components of the myosin and actin currents, respectively, and  $v_a^i$  and  $v_m^i$  the corresponding velocity components. The source/sink terms in the myosin equation correspond to a minifilament on-rate that depends upon actin (in a saturating form) and a density-dependent off-rate, with  $k$  the ‘bare’ ratio of these two quantities for  $\rho_a \gg \rho_a^h$ .

The continuity equations (1) and (2) are coupled by force balance conditions at the myosin-actin and actin-bilayer interfaces of our layered system (Fig. 2a), giving rise to constitutive relations for the currents:

$$J_m^i = \frac{\rho_m}{\rho_a} J_a^i - \rho_m \alpha([ATP]) P^i - \chi_m \nabla^i \rho_m, \quad (3)$$

and

$$J_a^i = \nabla_j \Sigma^{ij} - \chi_a \nabla^i \rho_a. \quad (4)$$

Here,  $\chi_a$  and  $\chi_m$  are the dimensionless inverse compressibilities for actin and myosin II minifilaments, respectively,  $\alpha([ATP])$  is a dimensionless coefficient that controls the ATP-dependence mini-filament velocities, and  $P^i$  is a polar order parameter. We assume that  $\alpha([ATP]) \rightarrow 1$  as  $[ATP] \rightarrow \infty$  [9]. The stress tensor  $\Sigma^{ij}$  is given by

$$\Sigma^{ij} = -\zeta(\rho_m, [ATP]) g^{ij} + \frac{1}{2} (P^i h^j - P^j h^i), \quad (5)$$

where  $\zeta$  is an active isotropic contractility, and  $g^{ij}$  is the inverse metric. The quantity  $h^i = -\delta \mathcal{F} / \delta P_i$ , is the so-called molecular field, which is derived from the elastic free-energy of the polarisation field [38]. Since elastic asymmetry between bend and splay had negligible effects on our results, we assume a one-constant Frank free energy

$$\mathcal{F} = \int \frac{\kappa}{2} |\nabla_i P^i|^2 dA, \quad (6)$$

where  $\kappa$ — the Frank elastic modulus [38]— is assumed to be small, so as to give a short actin persistence length comparable with experiments. The molecular field is thus given by  $h^i = \kappa \Delta P^i$ , where  $\Delta$  is the Laplacian.

The system of equations is closed by the dynamics of the polar order parameter, which is given by

$$D_t P^i = \frac{h^i}{\gamma} + \nu \left[ \frac{\rho_a}{\rho_a^*} (1 - P_j P^j) - (1 + P_j P^j) \right] P^i, \quad (7)$$

where  $\gamma$  controls the relaxation of  $P^i$ , and  $D_t P^i = \partial_t P^i + v_a^j \nabla_j P^i + \frac{1}{2} (\nabla^i v_{aj} - \nabla_j v_a^i) P^j$  is the objective

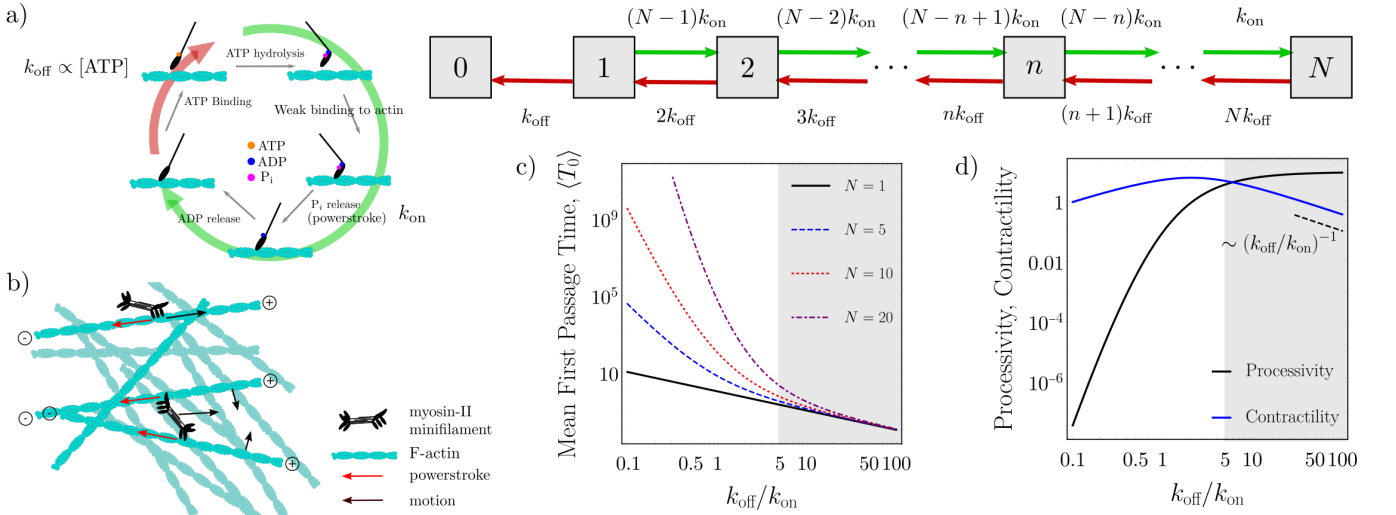


FIG. 3. **Myosin II minifilament kinetics.** **a)** Approximating the canonical 5-step ATP-cycle by a 2-step binding/unbinding process, the statistics of the bound status of a single myosin II minifilament's head-groups can be modelled using a ladder-like state space. **b)** The power-stroke associated with the transition between singly- and doubly-bound head-groups leads to processive 'steps' along actin filaments, additional bound head-groups leads to crosslinking and therefore meshwork remodelling that is contractile at the hydrodynamic scale (see [33–37]). **c)** As  $k_{\text{off}} \propto [\text{ATP}]$  increases, the MFPT until myosin II minifilament dissociation converges to  $\sim 1/k_{\text{off}}$ , irrespective of the total number of head-groups, permitting us to make the identification  $k \sim \langle T_0 \rangle^{-1}$ . **d)** The rate of processive (*i.e.*,  $1 \rightarrow 2$ ) and contractile (*i.e.*,  $n \rightarrow n+1$  for  $n \neq 1$ ) power-strokes scale as a constant and  $\sim 1/k_{\text{off}}$ , respectively, as  $k_{\text{off}} \propto [\text{ATP}]$  increases.

rate, or co-rotational derivative. The lyotropic term pre-multiplied by  $\nu$  gives the Landau-DeGennes transition as a function of order parameter density, such that for low actin density  $|P^i| \rightarrow 0$ , and at high densities  $|P^i| \rightarrow 1$  (SM Sec. 4 [19]).

Activity enters explicitly into our model in three places: the ratio  $k$ , which governs the binding kinetics of myosin II minifilaments [Eq. (1)]; the magnitude of isotropic contractile stresses  $\zeta$  [Eq. (5)], and; the magnitude,  $\alpha$ , of the monopolar-like processive force  $\propto P^i$  [Eq. (3)]. For the latter, we recall that, in this dimensionless presentation, a characteristic myosin minifilament velocity has been absorbed into the definitions of various quantities, and hence  $\alpha$  is a number between 0 and 1 (SM Sec. 4 [19]).

In principle, each of these active quantities, as well as passive dissipative coefficients and storage moduli, can depend on variables that are not treated hydrodynamically, such as the concentration of available ATP. Couplings of this type cannot be obtained from either (broken-)symmetries or the relevant conservation principles at play, and instead must be obtained either empirically or from a microscopic model.

#### IV. A MICROSCOPIC MODEL OF SINGLE MYOSIN II MINIFILAMENTS

To motivate how the different terms in our hydrodynamic description of actomyosin scale with the concen-

tration of available ATP, we examine a simple model that aims to capture the statistics of the bound status of the  $N \approx 50$  individual head groups that belong to a single myosin II minifilament.

We approximate the canonical five-step ATP cross-bridge cycle [3] by a two-step process where headgroups bind to actin with a constant rate  $k_{\text{on}}$ , and unbind with a rate  $k_{\text{off}} \propto [\text{ATP}]$  (Fig. 3a-b). Headgroups are assumed to act independently, neglecting any potential load dependence [39, 40] and/or mechanical cooperativity [41, 42]. When  $n$  headgroups are bound, therefore, the rate of an additional binding is simply  $(N - n)k_{\text{on}}$ , whilst the rate of unbinding is  $n k_{\text{off}}$ . This results in a ladder-like stochastic process of headgroup binding and unbinding that inevitably ends with myosin II minifilament dissociation (*i.e.*, no headgroups bound).

Notably, the master equation associated with the above process can be solved recursively to yield the mean first passage time to myosin II minifilament dissociation,  $\langle T_0 \rangle$ , having started with only one bound headgroup (SM Sec. 3 [19]). This demonstrates that higher concentrations of ATP increase the ratio of off- to on-rates and therefore decrease myosin II minifilament residence times, which is qualitatively in line with more complex models of myosin II minifilaments in the limit of low load [43, 44] and experimental observations of the duty ratio of myosin I proteins [45]. Specifically, for all appreciable levels of ATP,  $\langle T_0 \rangle \sim k_{\text{on}}/k_{\text{off}}$ , irrespective of the number of headgroups,  $N$ , in a given minifilament (Fig. 3c). Despite the fact that the minifilament population com-



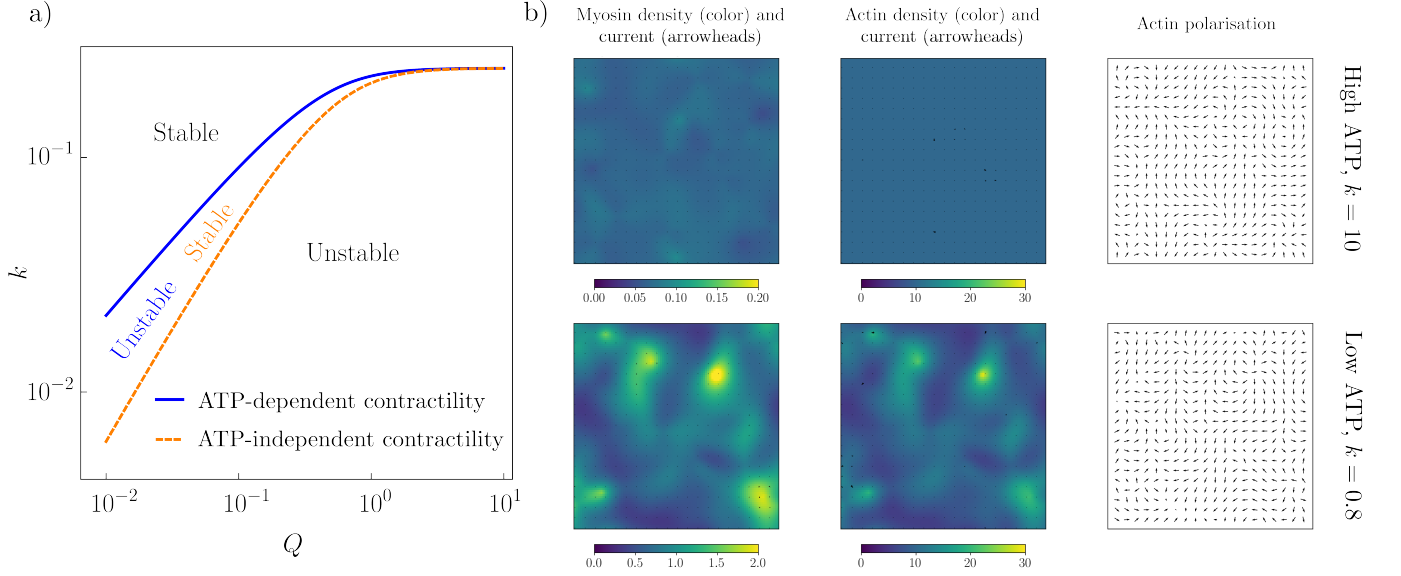


FIG. 4. **ATP-dependent advective-contractile instability.** **a)** Linear stability diagram for an ATP dependent and independent hydrodynamic theory as a function of magnitude of the wavevector,  $Q = \sqrt{|q|^2}$ , and dimensionless myosin-II minifilament unbinding rate,  $k$ . This shows the region where the ATP dependent version has a advective-contractile instability for higher values of  $k$  than would be expected in the ATP independent case. **b)** Numerical solutions of the hydrodynamic equations at high ( $k = 10$ ) and low ( $k = 0.8$ ) ATP concentrations/minifilament unbinding rate showing the non-linear evolution of the advective-contractile instability from uniform densities and random unit polarisation initial conditions on a  $10 \times 10$  grid. The timepoint is given by  $t = 24$  in dimensionless units. Both plots are made with the following parameters  $\kappa = 0.1$ ,  $\xi = -1$ ,  $\chi_a = 0.1$ ,  $\chi_m = 1$ ,  $\gamma = 10$ ,  $\nu = 1$ ,  $\rho_a^* = 5$  and  $\rho_a^h = 5$ . For further details on numerical solutions see [19].

prises oligomers of different lengths, we may therefore treat all minifilaments equally when referring to the dependence of their kinetics (*i.e.*, their residence times) on ATP. This means that the quantity  $k$ —the ‘bare’ ratio of mini-filament off- to on-rates—which appears in our hydrodynamic model, must scale with  $1/\langle T_0 \rangle$ , and hence  $k \propto [ATP]$ .

Extending this type of argument to active and passive coefficients, however, requires the distribution over the *number* of state transitions—*i.e.*, the likelihood that a given transition (*e.g.*,  $n \rightarrow n+1$ ) will occur a certain number of times. The reason is that each ascending transition in our model involves a single power-stroke, and therefore the mean number of such transitions divided by the total minifilament residence time can be used as a proxy for the rate at which work is done, or the power.

We make a distinction between transitions of the type  $1 \rightarrow 2$ , which are tantamount to taking a single processive step along the minifilament (towards the ‘plus’ end), and all other ascending transitions,  $n \rightarrow n+1$  for  $n \neq 1$ , which involve one or more bound headgroups in addition to that which performs the power-stroke. If these additional bound headgroups anchor the myosin II to either the same actin filament or another actin filament that cannot move due to meshwork frustration, then motion stalls. Otherwise, the ATP-induced power-stroke can generate relative motion between two or more actin filaments. At the scale of bulk hydrodynamic descriptions, this latter case manifests as predominantly

contractile forces, since the response of actin filaments is asymmetric when subjected to either compressive or tensile loads [33–36], and the dwell time of myosin II headgroups at the plus-end of actin filaments is abnormally long [37].

Using a sum-over-paths representation of our model (SM Sec. 3 [19]) the aforementioned proxies for the power associated with these two cases—‘processivity’ and ‘contractility’—can be calculated. These imply that, as ATP increases, the former converges to approximate a constant, whilst the latter scales like  $1/k$  (Fig. 3d). In the context of the hydrodynamic model, this leads us to make two assumptions. First, we assume that  $\zeta$  has the form

$$\zeta = \frac{\xi \rho_m}{k}. \quad (8)$$

Second, we assume that the mono-polar-like force that drives the processivity of myosin is of constant magnitude, and hence  $\alpha = 1$ .

## V. AN ATP-DEPENDENT ADVECTIVE-CONTRACTILE INSTABILITY

To understand the ramifications of our scaling ansatz, we perform a linear stability analysis of the resulting hydrodynamic theory under perturbations about a uniformly ordered-state, deep in the nematic phase (*i.e.*,

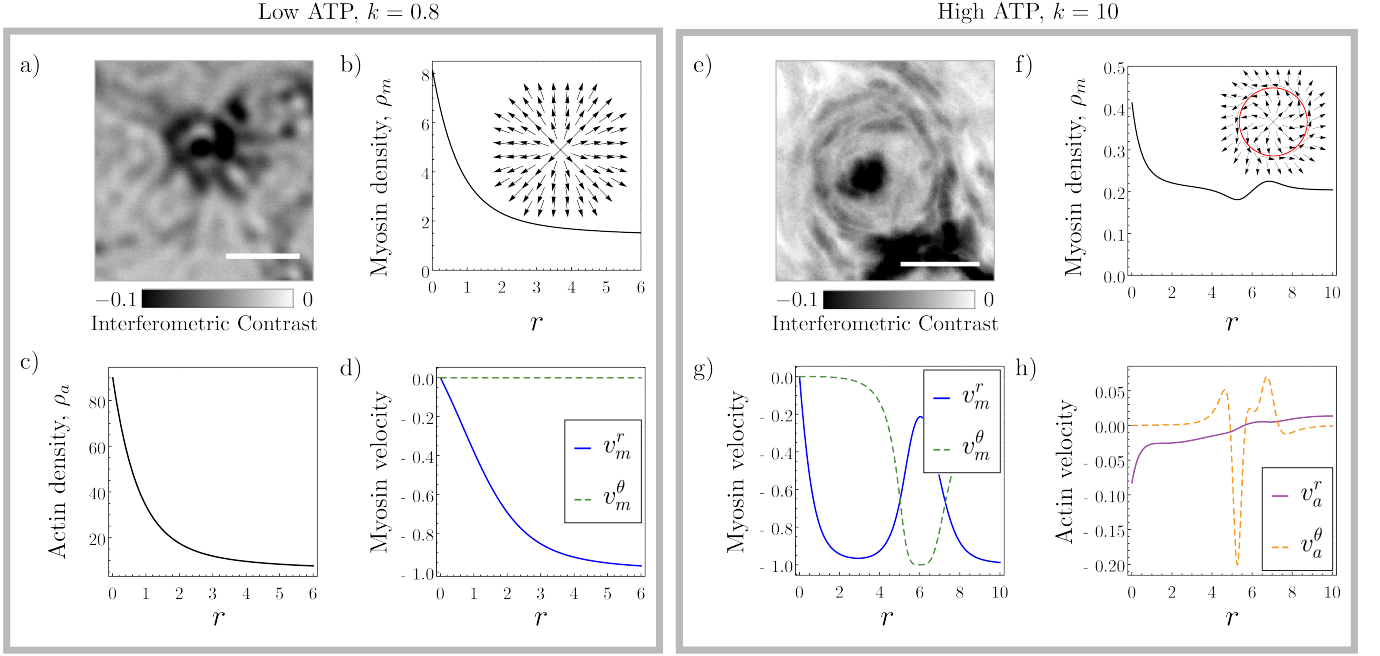


FIG. 5. **Comparing theory and experiment.** **a)** Static iSCAT microscopy image of an aster formed after depletion of ATP (20 min after addition of 0.1 mM ATP, where dark areas indicate high myosin II minifilament density (scale bar 2  $\mu\text{m}$ ). On add-back of ATP, myosin II minifilaments process towards the focus of the aster (see Vid. 9 and SM Sec. 2). This compares favourably with radial steady-state solutions for **b)** myosin density, **c)** actin density, and **d)** the myosin velocity (texture shown in **b** inset). **e)** Minimal intensity projection (over 120s) of a spiral-like structure captured using iSCAT (scale bar 2  $\mu\text{m}$ ) 10-15 min after addition of 0.1 mM ATP. Similarly, this compares well with radial **f)** myosin density and **g)** velocity profiles at zeroth order in  $\epsilon$  (texture shown in **f** inset). **h)** Radial actin velocity profile at  $O(\epsilon)$ . Panels **b-d** plotted for  $\xi = -1$ ,  $\chi_m = 1$ ,  $\chi_a = 0.1$ ,  $k = 0.8$ . Panels **f-h** plotted for  $\xi = -1$ ,  $\chi_m = 1$ ,  $\chi_a = 0.1$ ,  $k = 10$ ,  $a = 6$ ,  $R = 6$  and  $\kappa = 0.1$ .

disregarding the lyotropic term in the dynamics of the polarisation vector, and instead imposing  $P^i P_i = 1$  via a Lagrange multiplier).

Traditionally, active hydrodynamic descriptions of this type are characterised by an advective-contractile instability, whereby contraction of the actin meshwork advects the bound myosin II motors that are generating the contractile force, resulting in a form of advective feedback that can result in asterlike foci. However, in our case, the ATP-dependence of myosin II minifilament off-rates, as well that of the magnitude of active contractility, lead to some modifications. Specifically, each contribute a factor of  $k$  ( $\propto [\text{ATP}]$ ) to the linear stability condition, resulting in the following quadratic form:

$$-k - \left( \frac{\xi}{k^2 \rho_a^{(0)}} + \chi_m \right) Q^2 \geq 0, \quad (9)$$

which applies in the small wavevector,  $Q$ , regime, where  $\rho_a^{(0)}$  is the uniform background actin density (SM Sec. 6 [19]). To this order in  $Q$ , the criterion that there exists an unstable regime is then just given by  $k^2 < -\xi/\rho_a^{(0)} \chi_m$ , where the right-hand side is positive due to the sign convention that  $\xi$  is negative for contractility (and positive for extensility). That is, advective-contractile feedback is unstable beneath a threshold level of ATP concentration.

Of note, by plotting (9) as a function of  $Q$  and  $k$  (on log-log scale) alongside a similar condition, but where contractility is ATP-independent, we can show that, at low enough levels of ATP, a contractile instability can be triggered in a regime where it might otherwise be expected to be stable (Fig. 4b).

Despite this conceptual insight, such analysis is nevertheless performed around a uniformly ordered stable state, rather than the random ordering associated with the deposition of actin filaments in our experiments. We therefore numerically obtained full (non-linear) solutions to our equations on a periodic domain using a central space, RK4 time finite-difference method (SM Sec. 7 [19]). This not only verifies that our ATP-dependent heuristic for advective-contractile feedback holds in the wider setting of our experiments, but also serves to identify “low” and “high” regimes of  $k$  for which asters do and do not form, respectively, when starting from uniform densities with random orientation and unit magnitude polarization. Videos 10 & 11 show example solutions in high and low regimes, respectively, with corresponding stills from the long time limit shown in Fig. 4b. As expected, in the high ATP case, the actin and myosin densities remain approximately uniform as the polarization relaxes, and no contractile instability occurs. In the low ATP case, however, an advective-contractile instability occurs and dense actin and myosin clusters form around

+1 topological defects (aster or spiral like structures). These structures eventually coarsen to a single aster-like defect where the coarsening time depends on the domain size.

## VI. COMPARISON OF STEADY STATES BETWEEN THEORY AND EXPERIMENT

Both our analysis and numerical solutions are suggestive that an ATP-dependent criterion for advective-contractile feedback codifies how actomyosin remodelling changes as ATP depletes. This assertion is further supported by looking for steady-state and quasi-steady-state solutions to our equations and comparing them with our observations (SM Sec. 5 [19]).

At low levels of ATP,  $k$  is small, and therefore the magnitude of the active contractile term that appears in (4) via the stress tensor (5) is large. In this case, an axisymmetric steady-state solution to Eqs. (2) and (7) is just a radial aster-like actin texture that is stationary (*i.e.*,  $\vec{P} = \vec{e}_r$  and  $\vec{v}_a = \vec{0}$ ). Since the molecular field is zero in this case, this implies that  $\vec{v}_m$  is a function of  $\rho_m$ , such that the accumulation of myosin II minifilaments due to their procession towards the texture's centre is balanced by the density dependent dissociation rate (see Vid. 9 and SM Sec. 2 for this behaviour in experiment [19]). Solving this boundary value problem for  $\rho_m$  requires a shooting method. The solution can nevertheless be substituted into the remaining force balance condition, which equates contractile forces with those resisting the compression of actin. This gives a first order equation for  $\rho_a$  that is readily solvable numerically (SM Sec. 4 [19]). The resulting aster-like steady-state is depicted in Fig. 5b-d. Since it is qualitatively independent of  $k$ , we expect that the system converges to this state as ATP depletes.

By contrast, at intermediate-to-high ATP,  $k$  is large, and so active contractile stresses are small. Since we further assume both the elastic modulus,  $\kappa$ , and the inverse compressibility,  $\chi_m$ , are small, this implies that the velocity of actin,  $\vec{v}_a$ , is also small. We may therefore use a perturbative approach to characterise the system in this regime, expanding in  $\epsilon = 1/k$ , and solving hierarchically.

At zeroth order,  $\vec{v}_a^{(0)} = 0$ , implying freedom to impose  $\vec{P}^{(0)}$  and  $\rho_a^{(0)}$ . To mimic experimental motifs, we choose a spiral texture

$$\vec{P}^{(0)} = \frac{r(R^2 - r^2)^2 \vec{e}_r + \frac{a^3 r^5}{(r+R)^3} \vec{e}_\theta}{\sqrt{\left(\frac{a^3 r^5}{(r+R)^3}\right)^2 + r^2 (R^2 - r^2)^4}}, \quad (10)$$

with density profile  $\rho_a^{(0)} = cr^2 e^{-r^2/w} + l$  (SM Sec. 5 [19]). In this case, the myosin II minifilament velocity profile,  $\vec{v}_m$  is that which balances propulsive forces with density gradients. Substituting into (1), the resulting boundary value problem is again solvable via a shooting method. The results are in-line with experimental observations,

with an inward flux of myosin II minifilaments giving way to a circular motion around a central foci, at which point the high densities are balanced by high dissociation rates.

As might be expected, this state is unstable at first order in  $\epsilon$ . We can, nevertheless, calculate first order corrections to the actin velocity profile,  $\vec{v}_a^{(1)}$ . In addition to radial corrections, this results in a small circular flow in the same direction as the myosin II minifilaments (a phenomenon also seen in experiments, Fig. 2e & SM Sec. 2 [19]) that is accompanied by a slight shear-banding. The former is consistent with our observations, whilst the latter is either not present, or cannot be observed at the present resolution.

## VII. DISCUSSION

When taken together, experiments, single myosin II minifilament kinetics, and bulk hydrodynamics are all consistent with the notion that a change in the concentration of available ATP not only changes the power of actomyosin, but it can also change the mode by which work is done. Here, we have argued that, as the concentration of available ATP decreases, the processivity of myosin II minifilaments gives way to isotropic contractile forces. The reason is that the hydrolysis cycle by which chemical energy, in the form of ATP, is transduced into mechanical work involves, as an intermediate step, the unbinding of individual headgroups from actin. As a result, increased levels of ATP reduce the likelihood that a given myosin II minifilament spans more than one actin filament, therefore reducing the ability for the generation of contractile forces, and instead resulting in an increased likelihood of processive motion. This heuristic is codified in an ATP-dependent criterion for advective-contractile feedback, the onset of which, as ATP depletes, we propose as the underlying mechanism that dictates a non-trivial relationship between power and remodelling.

From a theoretical perspective, our work highlights the importance of understanding the functional form of both active and passive coefficients, and the possibility that even simple microscopic models can provide interesting insight and scaling hypotheses. This is relevant because a variety of other active hydrodynamic models, such as those used to study active turbulent-like flows, for example, predict scaling laws that are *non-universal*, *i.e.*, they depend of the values of the coefficients in the theory [46–50].

From a biological perspective, this demonstrates how to encode local biochemistry that, whilst not necessarily hydrodynamic, can nevertheless be crucial to function. We speculate that our findings may be important for the generic understanding of how actomyosin remodelling is regulated. That is, in addition to phosphorylation-driven molecular signalling pathways as the canonical mechanism behind the regulation of myosin II activity and/or actin filament growth, ATP concentration may also be

important, suggesting a link between essential functions such as contraction or shape change and the metabolic pathways by which ATP is synthesized. Such ideas may even prove relevant to understand the ramifications of a compromised metabolism [51, 52].

There remain several aspects of our theory and analysis that might be extended. For the microscopic modelling, corrections to consider the potential effects of load-dependence [39, 43], cooperativity [41, 42] and chirality [53], could lead to quantitative manifestations of such effects at the hydrodynamic level. From a hydrodynamic perspective, the main current challenge is to extend current liquid crystal-like nemato-hydrodynamic descriptions to describe the remodelling of transient networks of intermediate-to-long actin filaments, which are semi-flexible and curved on length-scales similar to the filaments themselves. Whilst such networks have been explored extensively in numerical simulations—particularly in terms of rigidification transitions and contractility generation [6, 33, 54–62]—writing down a constitutive relation for such materials is a significant outstanding challenge in the field. To our knowledge, it has only been attempted at the level of bulk passive rheology thus far, and has no straightforward generalisation to active systems [63–65]. Amongst other things, such a constitutive relation would need to account for the known shear-stiffening of actomyosin under imposed strain [33]. The Poisson bracket approach for computing reactive couplings in generalised hydrodynamics might prove useful here, as in nematic polymer theory [29, 66].

Regarding our experimental observations, we remark that whilst the formation of vortices and spirals have been noted in microtubule-based systems [67], similar works on actomyosin networks did not report such structures [6, 8, 14, 35, 36, 60]. This presents an open ques-

tion: how precisely do the remarkably persistent vortex- and spiral-like structures that we observe depend on the experimental conditions? Possible factors here include: a relatively low actin filament concentration (equivalent to  $[G\text{-actin}] = 125 \text{ nM}$  compared to  $[G\text{-actin}] > 1 \mu\text{M}$  in other works) which leads to very thin f-actin layers ( $< 6$  filaments) [9]; the absence of crowding factors; the minimisation of laser induced photo-damage by using label-free imaging, and; degassed buffers in combination with an oxygen scavenger system, which decrease the generation of dead heads in myosin II minifilaments that would lead to irreversible crosslinking [60].

In conclusion, we believe that our work highlights a novel conceptual advance: ATP is more than ‘just’ a fuel, it impacts the mode by which actomyosin remodels, as well as the rate. In this context, developing more precise experimental setups (*e.g.*, microfluidic control and maintenance of ATP concentrations), more realistic microscopic theories to feed into coarse-grained hydrodynamic parameters, and extending current liquid crystal-like constitutive relations that capture the rheology of transient cross-linked networks are just three of the possible directions future research in this area could take.

#### ACKNOWLEDGMENTS

RGM and SCA-I acknowledge funding from the EMBL-Australia program. DVK thanks Phillip Kukura and Nicolas Hundt for enabling the iSCAT experiments, Mohan Balasubramanian for access to the TIRF microscope, and the Wellcome-Warwick Quantitative Biomedicine Programme for funding (Wellcome Trust ISSF, RMRCB0058). SCA-I would like to thank Jack Binysh for helpful comments and suggestions.

- 
- [1] S. Banerjee, M. L. Gardel, and U. S. Schwarz, Annual Review of Condensed Matter Physics **11**, 031218 (2020).
  - [2] J. Prost, F. Jülicher, and J.-F. Joanny, Nature Physics **11**, 111 (2015).
  - [3] B. Alberts, A. Johnson, J. Lewis, M. Raff, K. Roberts, and P. Walter, *Molecular Biology of the Cell*, 4th ed. (Garland Science, 2002).
  - [4] M. C. Marchetti, J. F. Joanny, S. Ramaswamy, T. B. Liverpool, J. Prost, M. Rao, and R. A. Simha, Reviews of Modern Physics **85**, 1143 (2013).
  - [5] M. J. Tyska and D. M. Warshaw, Cell Motility **51**, 1 (2002).
  - [6] D. Smith, F. Ziebert, D. Humphrey, C. Duggan, M. Steinbeck, W. Zimmermann, and J. Käs, Biophysical Journal **93**, 4445 (2007).
  - [7] D. Mizuno, C. Tardin, C. F. Schmidt, and F. C. MacKintosh, Science **315**, 370 (2007).
  - [8] S. K. Vogel, Z. Petrusek, F. Heinemann, and P. Schwill, eLife **2**, e00116 (2013).
  - [9] L. S. Mosby, N. Hundt, G. Young, A. Fineberg, M. Polin, S. Mayor, P. Kukura, and D. V. Köster, Biophysical Journal **118**, 1946 (2020).
  - [10] J. Ortega-Arroyo and P. Kukura, Physical Chemistry Chemical Physics **14**, 15625 (2012).
  - [11] D. Cole, G. Young, A. Weigel, A. Sebesta, and P. Kukura, ACS Photonics **4**, 211 (2017).
  - [12] Y. Sumino, K. H. Nagai, Y. Shitaka, D. Tanaka, K. Yoshikawa, H. Chaté, and K. Oiwa, Nature **483**, 448 (2012).
  - [13] T. Sanchez, D. T. N. Chen, S. J. DeCamp, M. Heymann, and Z. Dogic, Nature **491**, 431 (2012).
  - [14] D. V. Köster, K. Husain, E. Iljazi, A. Bhat, P. Bieling, R. D. Mullins, M. Rao, and S. Mayor, Proceedings of the National Academy of Sciences **113**, E1645 (2016).
  - [15] D. V. Köster and S. Mayor, Current Opinion in Cell Biology **38**, 81 (2016).
  - [16] M. Fritzsche, R. A. Fernandes, V. T. Chang, H. Colin-York, M. P. Clausen, J. H. Felce, S. Galiani, C. Er-lenkämper, A. M. Santos, J. M. Heddleston, I. Pedrosa-Pacheco, D. Waithe, J. B. de la Serna, B. C. Lagerholm, T.-l. Liu, T.-L. Chew, E. Betzig, S. J. Davis, and C. Eggeling, Science Advances **3**, e1603032 (2017).

- [17] J. Spudich and S. Watts, *J. Biol. Chem.* **246**, 4866 (1971).
- [18] T. D. Pollard, in *Methods in Cell Biology*, The Cytoskeleton Part A. Cytoskeletal Proteins, Isolation and Characterization, Vol. 24, edited by L. Wilson (Academic Press, 1982) pp. 333–371.
- [19] “Electronic supplementary material can be found at: ..... detailing additional figures, experimental details & calculations.”.
- [20] W. Thielicke, *The Flapping Flight of Birds - Analysis and Application*, Ph.D. thesis, Rijksuniversiteit Groningen (2014).
- [21] W. Thielicke and E. Stamhuis, *Journal of Open Research Software* **2**, e30 (2014), number: 1 Publisher: Ubiquity Press.
- [22] D. Garcia, *Experiments in fluids* **50**, 1247 (2011).
- [23] Y. Tanaka, A. Ishijima, and S. Ishiwata, *Biochimica et Biophysica Acta (BBA) - Protein Structure and Molecular Enzymology* **1159**, 94 (1992).
- [24] T. Nishizaka, T. Yagi, Y. Tanaka, and S. Ishiwata, *Nature* **361**, 269 (1993).
- [25] E. M. De La Cruz, J. Roland, B. R. McCullough, L. Blanchoin, and J.-L. Martiel, *Biophysical Journal* **99**, 1852 (2010).
- [26] K. Kruse, J. F. Joanny, F. Jülicher, J. Prost, and K. Sekimoto, *Physical Review Letters* **92**, 078101 (2004).
- [27] A. Das, A. Bhat, R. Sknepnek, D. Köster, S. Mayor, and M. Rao, *Science Advances* **6**, eaay6093 (2020).
- [28] E. Meijering, M. Jacob, J.-C. F. Sarria, P. Steiner, H. Hirling, and M. Unser, *Cytometry Part A* **58A**, 167 (2004).
- [29] P. Chaikin and T. Lubensky, *Principles of Condensed Matter Physics* (Cambridge University Press, 2000).
- [30] K. Kruse, J. F. Joanny, F. Jülicher, J. Prost, and K. Sekimoto, *The European Physical Journal E* **16**, 5 (2005).
- [31] K. Husain and M. Rao, *Physical Review Letters* **118**, 078104 (2017).
- [32] K. Gowrishankar and M. Rao, *Soft Matter* **12**, 2040 (2016).
- [33] G. H. Koenderink, Z. Dogic, F. Nakamura, P. M. Bendix, F. C. MacKintosh, J. H. Hartwig, T. P. Stossel, and D. A. Weitz, *Proceedings of the National Academy of Sciences* **106**, 15192 (2009).
- [34] I. Linsmeier, S. Banerjee, P. W. Oakes, W. Jung, T. Kim, and M. P. Murrell, *Nature Communications* **7**, 12615 (2016).
- [35] M. P. Murrell and M. L. Gardel, *Proceedings of the National Academy of Sciences* **109**, 20820 (2012).
- [36] Y. Ideses, A. Sonn-Segev, Y. Roichman, and A. Bernheim-Groswasser, *Soft Matter* **9**, 7127 (2013).
- [37] V. Wollrab, J. M. Belmonte, L. Baldauf, M. Leptin, F. Nédélec, and G. H. Koenderink, *Journal of Cell Science* **132**, jcs219717 (2019).
- [38] P. de Gennes and J. Prost, *The Physics of Liquid Crystals*, International Series of Monogr (Clarendon Press, 1993).
- [39] E. P. Debold, J. B. Patlak, and D. M. Warshaw, *Biophysical Journal* **89**, L34 (2005).
- [40] S. Stam, J. Alberts, M. Gardel, and E. Munro, *Biophysical Journal* **108**, 1997 (2015).
- [41] S. Walcott, D. Warshaw, and E. Debold, *Biophysical Journal* **103**, 501 (2012).
- [42] M. Kaya, Y. Tani, T. Washio, T. Hisada, and H. Higuchi, *Nature Communications* **8**, 16036 (2017).
- [43] T. Erdmann, K. Bartelheimer, and U. S. Schwarz, *Physical Review E* **94**, 052403 (2016).
- [44] P. J. Albert, T. Erdmann, and U. S. Schwarz, *New Journal of Physics* **16**, 093019 (2014).
- [45] C. Veigel, L. M. Coluccio, J. D. Jontes, J. C. Sparrow, R. A. Milligan, and J. E. Molloy, *Nature* **398**, 530 (1999).
- [46] B. Martínez-Prat, R. Alert, F. Meng, J. Ignés-Mullol, J.-F. Joanny, J. Casademunt, R. Golestanian, and F. Sagués, *Physical Review X* **11**, 031065 (2021).
- [47] L. Giomi, *Physical Review X* **5**, 031003 (2015).
- [48] R. Alert, J. Casademunt, and J.-F. Joanny, *Annual Review of Condensed Matter Physics* **13**, 143 (2022).
- [49] J. Dunkel, S. Heidenreich, K. Drescher, H. H. Wensink, M. Bär, and R. E. Goldstein, *Physical Review Letters* **110**, 228102 (2013).
- [50] S. P. Thampi, R. Golestanian, and J. M. Yeomans, *Philosophical Transactions of the Royal Society A: Mathematical, Physical and Engineering Sciences* **372**, 20130366 (2014).
- [51] M. A. Jansen, H. Shen, L. Zhang, P. E. Wolkowicz, and J. A. Balschi, *American Journal of Physiology-Heart and Circulatory Physiology* **285**, H2437 (2003).
- [52] N. Smith and E. Crampin, *Progress in Biophysics and Molecular Biology* **85**, 387 (2004).
- [53] Y. H. Tee, T. Shemesh, V. Thiagarajan, R. F. Hariadi, K. L. Anderson, C. Page, N. Volkmann, D. Hanein, S. Sivaramakrishnan, M. M. Kozlov, and A. D. Bershadsky, *Nature Cell Biology* **17**, 445 (2015).
- [54] D. A. Head, A. J. Levine, and F. C. MacKintosh, *Physical Review E* **68**, 061907 (2003).
- [55] D. A. Head, A. J. Levine, and F. C. MacKintosh, *Physical Review Letters* **91**, 108102 (2003).
- [56] K. Kasza, C. Broedersz, G. Koenderink, Y. Lin, W. Messner, E. Millman, F. Nakamura, T. Stossel, F. MacKintosh, and D. Weitz, *Biophysical Journal* **99**, 1091 (2010).
- [57] B. Stuhmann, M. Soares e Silva, M. Depken, F. C. MacKintosh, and G. H. Koenderink, *Physical Review E* **86**, 020901 (2012).
- [58] T. H. Tan, M. Malik-Garbi, E. Abu-Shah, J. Li, A. Sharma, F. C. MacKintosh, K. Keren, C. F. Schmidt, and N. Fakhri, *Science Advances* **4**, eaar2847 (2018).
- [59] Y. Mulla, F. MacKintosh, and G. H. Koenderink, *Physical Review Letters* **122**, 218102 (2019).
- [60] J. Alvarado, M. Sheinman, A. Sharma, F. C. MacKintosh, and G. H. Koenderink, *Nature Physics* **9**, 591 (2013).
- [61] S. Arzash, P. M. McCall, J. Feng, M. L. Gardel, and F. C. MacKintosh, *Soft Matter* **15**, 6300 (2019).
- [62] F. Nédélec and D. Foethke, *New Journal of Physics* **9**, 427 (2007).
- [63] F. Tanaka and S. F. Edwards, *Macromolecules* **25**, 1516 (1992).
- [64] F. Tanaka and S. F. Edwards, *Journal of Non-Newtonian Fluid Mechanics* **43**, 273 (1992).
- [65] F. Tanaka and S. F. Edwards, *Journal of Non-Newtonian Fluid Mechanics* **43**, 247 (1992).
- [66] R. Kamien, *Physical Review E* **61**, 2888 (2000).
- [67] F. J. Nédélec, T. Surrey, A. C. Maggs, and S. Leibler, *Nature* **389**, 305 (1997).
- [68] S. Budnar, K. B. Husain, G. A. Gomez, M. Naghibosadat, A. Varma, S. Verma, N. A. Hamilton, R. G. Morris, and A. S. Yap, *Developmental Cell* **49**, 894 (2019).



## SUPPLEMENTARY INFORMATION

### 1. Experimental Methods

#### *a. Purified Proteins*

Actin was purified from chicken breast following the protocol from Spudich and Watt [17] and kept on ice in monomeric form in G-buffer (2 mM Tris Base, 0.2 mM ATP, 0.5 mM TCEP-HCl, 0.04% NaN<sub>3</sub>, 0.1 mM CaCl<sub>2</sub>, pH 7.0); for TIRF microscopy experiments, G-actin was labelled with Maleimide-Alexa488 as described earlier [14]. The experiments using iSCAT microscopy were performed with myosin II obtained from chicken breast following a modified protocol from Pollard [18] and kept in monomeric form in myo-buffer (500 mM KCl, 1 mM EDTA, 1 mM DTT, 10 mM HEPES, pH 7.0). For TIRF microscopy experiments, myosin II was purchased (rabbit m. psoas, Hypermol, #8306-01). The day prior to experiments, functional myosin II proteins were separated from proteins containing dead head domains by a round of binding and unbinding to F-actin at a 5 : 1 actin to myosin ratio (switch from no ATP to 3 mM ATP) followed by a spin at 60,000 rpm for 10 min at 4°C in a TLA100.3 rotor. The supernatant containing functional myosin II was dialyzed against myo-buffer over-night at 4°C and could be used for up to three days when stored at 4°C.

To control the length of actin filaments, we titrated purified murine capping protein to the actin polymerization mix. The purification of capping protein was described earlier [14]. To link actin to the SLB, we used a construct containing 10x His domains followed by a linker (KCK) and the actin binding domain of Ezrin (HKE) as described earlier [14]. For TIRF experiments, we expressed and purified His10-SNAP-Ezrin actin binding domain (HSE) and labelled it with SNAP-surface 549 (New England BioLabs Inc., #S91112S) following the manufacturer's protocol.

#### *b. Supported Lipid Bilayer and Experimental Chamber Preparation*

Experimental chambers were prepared, and supported lipid bilayers (SLB) containing 98% DOPC and 2% DGS-NTA(Ni<sup>2+</sup>) lipids were formed as described earlier [14] in chambers filled with 100  $\mu$ l KMEH (50 mM KCl, 2 mM MgCl<sub>2</sub>, 1 mM EGTA, 20 mM HEPES, pH 7.2). SLB formation was observed live using iSCAT microscopy, to ensure that a fluid lipid bilayer formed without holes [9].

#### *c. Formation of Acto-Myosin Network*

In a typical experiment, SLBs were formed, incubated with 10 nM HKE for 40 min, and washed thrice with KMEH. During this incubation time, F-actin was polymerized. First, 10%vol of 10 $\times$  ME buffer (100 mM MgCl<sub>2</sub>, 20 mM EGTA, pH 7.2) were mixed with the G-actin stock (for TIRF experiments unlabelled G-actin was supplemented with 10% of Alexa488-labeled G-actin) and incubated for 2 min to replace G-actin bound Ca<sup>2+</sup> ions with Mg<sup>2+</sup>. Addition of 2 $\times$  KMEH buffer, supplemented with 2 mM Mg-ATP, induced F-actin polymerization at a final G-actin concentration of 5  $\mu$ M. After 20 – 30 min incubation, the desired amount of F-actin was added to the SLBs using blunt cut 200  $\mu$ l pipette tips. An incubation of 30 min allowed the F-actin layer to bind to the SLB at steady-state. For the addition of myosin II filaments to the sample, intermediate dilutions of myosin II proteins were prepared in milliQ water at 10x the final concentration from fresh myosin II stock (4mM, 500mM KCl) in a test tube and incubated for 5 min to allow the myosin II filament formation. Then, 1/10 of the sample buffer was replaced with the myosin II filament solution and supplemented with Mg-ATP (100 mM) at 0.1 mM final concentration. Afterwards, the evolution of the acto-myosin system was observed for up to 60 min. Typically, the system showed a remodelling behaviour for the first 10 – 15 min before contraction and aster formation started (due to ATP concentrations below 10  $\mu$ M as estimated from the activity of myosin II and earlier reports [6]). Once, the system reached a static, jammed state and no myosin activity could be observed, the system could be reset into a remodelling state by addition of Mg-ATP (100 mM) to a final concentration of 0.1 mM. Each step of this procedure was performed on the microscope stage, which allowed us to check its state continuously. The open chamber design allowed the addition of each component without inducing flows that would perturb the actin network. All experiments were performed at room temperature (22°C) and evaporation of buffer was minimal (< 5%vol). Details about the actin, myosin and ATP concentrations used in each experiment can be found in Table I.

Figure	[Actin]/nM	[CP]/nM	[Myosin II]/nM	[ATP]initial/ $\mu$ M	anti-bleach agent	$L_{F-actin}/\mu$ m
iSCAT experiments	300	0.38	100	100		$7 \pm 3.5$
TIRF experiments	200	0.25	10	100	PCA/PCD	$7.2 \pm 1.5$
	200	0.25	40	100	PCA/PCD	$7.2 \pm 1.5$
	250	0.25	20	100	PCA/PCD	$7.2 \pm 1.5$
	250	0.25	10	100	PCA/PCD	$7.2 \pm 1.5$

TABLE I. Summary of the experimental conditions (final concentrations in the imaging chamber).

*d. iSCAT microscope*

Interferometric scattering microscopy was performed on two different custom setups similar to those detailed in [10, 11]. Briefly, a weakly focused laser beam was scanned across the sample over an area  $32.6 \times 32.6 \mu\text{m}^2$  (635 nm laser). The light reflected from the glass-water interface together with the scattered light from the sample was imaged by a CMOS camera (MV-D1024-160-CL-8, Photonfocus, Switzerland). The cameras were controlled using custom LabVIEW software. The videos were recorded at 5 fps (635 nm laser) with the illumination intensity on the sample (635 nm laser:  $1.9 \text{ kW cm}^{-2}$ ) set to nearly saturate the camera with the returning light. The pixel size was 31.8 nm/pixel.

*e. Total Internal Reflection Fluorescence (TIRF) microscopy*

TIRF microscopy on acto-myosin networks containing Alexa488 labelled actin and SNAP-surface 549 labelled HSE were performed on a Nikon Ti Eclipse microscopy equipped with a Nikon TIRF laser coupler, 488nm, 563nm and 640nm lasers, a triple pass TIRF dichroic mirror (488nm, 549nm, 640nm; Chroma), a  $100\times$  (1.49NA) Nikon objective and 520 ( $\pm 5$ ) nm, 615 ( $\pm 5$ ) nm emission filters (Chroma). Images were recorded with an Zyla sCMOS camera (Andor) controlled by iQ3.0 software (Andor) and the pixel size was 63.4nm. To limit photodamage, we degassed buffers, employed a radical scavenger system (protocatechuic acid and Protocatechuate 3,4-Dioxygenase, Sigma) and reduced laser intensities to a minimum while imaging the sample only at 5s per frame.

*f. Image processing (iSCAT)*

Non-sample-specific illumination inhomogeneities, fixed-pattern noise and constant background were removed from the raw images by dividing each of them with a flat field image that contained only these features. The flat field image was computed by recording 2000 frames of the sample while moving the stage. For each pixel, a temporal median was calculated, resulting in a flat field image that only contained static features.

*g. Median filtering*

Movies were median filtered using MATLAB (MathWorks, Natick, MA, USA). For each image sequence, the median is computed for each pixel, deleted from the original image sequence and the median filtered image sequence as well as the computed median filter are saved.

*h. Actin filament length measurements*

Image stacks of actin filaments landing on the HKE decorated SLBs were taken at 10 Hz immediately after addition of actin filaments to the sample. Theses image stacks were split in segments of 10s and the median of each segment was subtracted from its last frame, to visualize freshly landed, isolated actin filaments. The images were then converted from the 32-bit interferometric contrast values to 8-bit (by the formula  $f(x) = -1000x + 1000$ ), bandpass filtered (low pass: 3 pixel, high pass: 20 pixel) and analysed with the image J plugin Neuron J [28]. Images of fluorescent actin

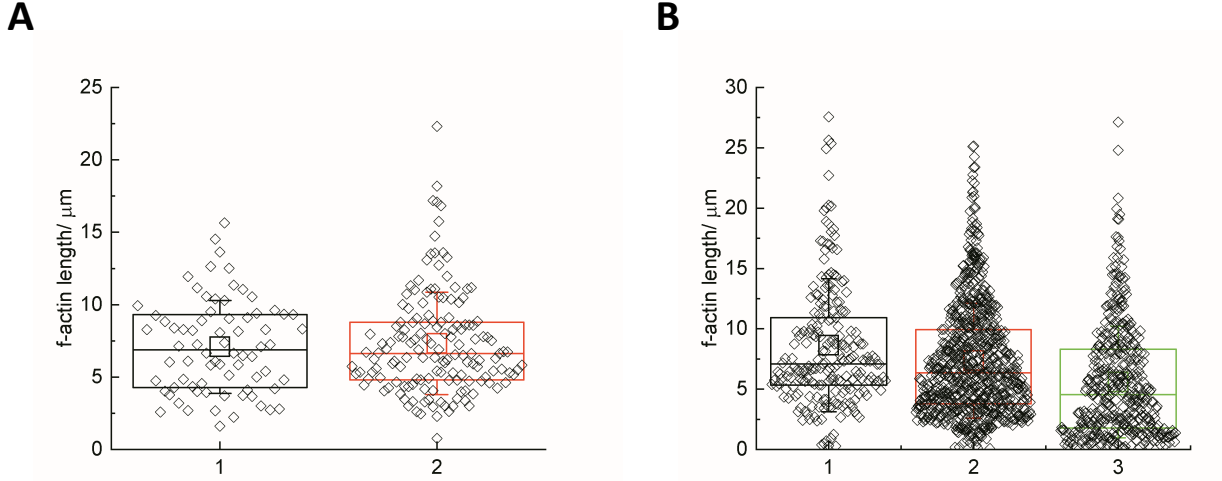


FIG. S1. A) Box plot of actin filament lengths measured from the batches used in iSCAT experiments ( $N = [74, 151]$ ). B) Box plot of actin filament lengths measured from the batch used for the three individual TIRF experiments ( $N = [218, 794, 422]$ ).

filaments landing on HSE decorated SLBs shortly after their addition to the sample were directly converted to 8-bit and analyzed with Neuron J.

### *i. Particle Image Velocimetry*

Particle Image Velocimetry (PIV) was performed using PIVlab [20–22]. Median filtered image sequences originating from iSCAT experiments were inverted as described above and transformed into 8-bit format using Image J. Image sequences from TIRF experiments were median filtered and directly converted into 8-bit format using image-J. The PIV vector maps were computed with the FFT window deformation algorithm and window sizes of 64, 32 and 16 pixels with step sizes of 32, 16 and 8 pixels for iSCAT experiments, and window sizes of 32 and 16 pixels with step sizes of 16 and 8 pixels for TIRF experiments, respectively. The accepted range of velocity vectors was limited to  $\pm 2 \mu\text{m s}^{-1}$ .

## **2. Additional Experimental Data & Figures**

### *a. Additional Figures*

In this section we show additional figures of actin filament lengths in iSCAT and TIRF experiments Fig. S1A)& B) respectively, PIV for an aster/foci Fig. S2, PIV vortices and spirals in the iSCAT data Fig. S3, PIV for vortices and spirals in the TIRF data Fig. S4 and wideview minimal intensity/standard deviation plots for the iSCAT Fig. S5.

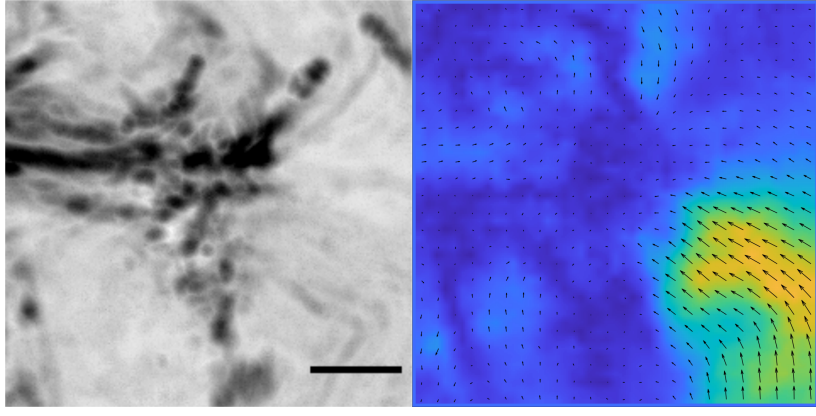


FIG. S2. Left: example of dynamics within an actomyosin aster/foci visualized by iSCAT with a minimal projection of differential images over a period of 120 s. Right: the corresponding averaged velocity maps computed with PIV. Scale bar  $2\ \mu\text{m}$ .

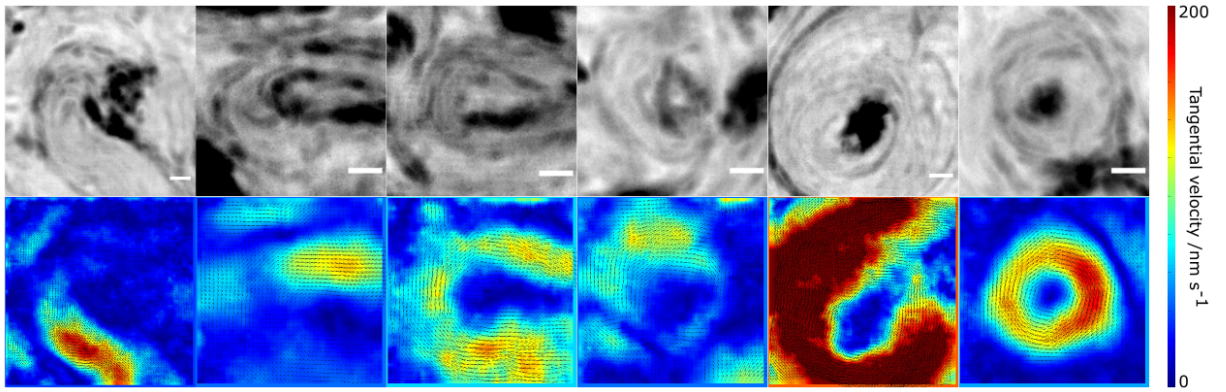


FIG. S3. Top: examples of dynamics within an actomyosin vortex and spirals visualized by iSCAT with a minimal projection of differential images over a period of 120 s. Bottom: the corresponding averaged velocity maps computed with PIV. Scale bars  $2\ \mu\text{m}$ .

#### *b. Captions for Extended Data (Videos)*

**Video 1** - iSCAT wide-view contractile foci/asters showing the contraction of the actomyosin network as ATP depletes.  $5\ \mu\text{m}$  scale bar.

**Video 2** - iSCAT wide-view showing vortex and spiral-like motifs. This movie corresponds to the stills from Fig. S5.  $5\ \mu\text{m}$  scale bar.

**Video 3** - iSCAT showing myosin mini-filaments (dark) swirling around and into the centre of a spiral-like structure. Motion is in a clockwise direction.  $2\ \mu\text{m}$  scale bar.

**Video 4** - iSCAT showing myosin mini-filaments (dark) swirling around and into the centre of a spiral-like structure. Motion is in a clockwise direction.  $2\ \mu\text{m}$  scale bar.

**Video 5** - iSCAT showing myosin mini-filaments (dark) swirling around the centre of a vortex-like structure. Motion is in a clockwise direction.  $2\ \mu\text{m}$  scale bar.

**Video 6** - iSCAT video showing two clusters fusing together to form a single foci.  $2\ \mu\text{m}$  scale bar.

**Video 7** - TIRF wide-view showing vortex-like swirling motion (after 40mins of incubation and then imaging immediately after an ATP add-back).  $5\ \mu\text{m}$  scale bar.

**Video 8** - TIRF showing the fluorescently labelled actin (L) and fluorescently labelled ezrin (membrane actin crosslinker) (R).  $2\ \mu\text{m}$  scale bar.

**Video 9** - Close up of myosin flowing into foci/aster-like structure showing that myosin precesses into the centre of the structure. iSCAT video after subtraction of the median signal to highlight the myosin filaments precessing into the centre of the aster-like structure.  $2\ \mu\text{m}$  scale bar.

**Video 10** - Numerical solution of active hydrodynamics at High ATM ( $k = 10$ ). Other parameters are given by:

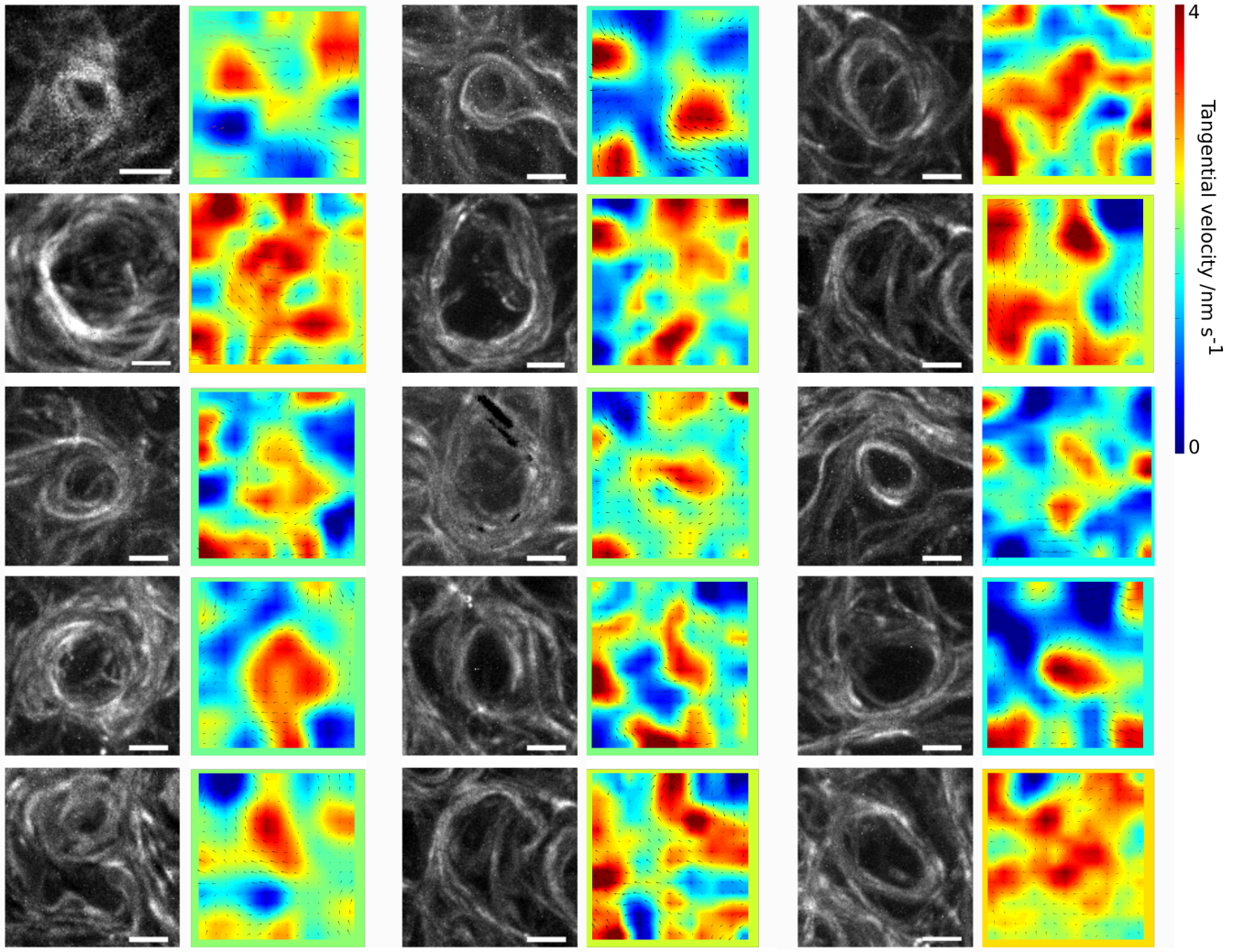


FIG. S4. Examples of actin dynamics within an acto-myosin vortex visualized by TIRF with a maximum projection of differential images over a period of 120 s and the corresponding averaged velocity maps computed with PIV; scale bar 2  $\mu\text{m}$ .

$\kappa = 0.1$ ,  $\xi = -1$ ,  $\chi_a = 0.1$ ,  $\chi_m = 1$ ,  $\gamma = 10$ ,  $\nu = 1$ ,  $\rho_a^* = 5$  and  $\rho_a^h = 5$ . See Sec. 7 for details.

**Video 11** - Numerical solution of active hydrodynamics at Low ATM ( $k = 0.8$ ). Other parameters are given by:  $\kappa = 0.1$ ,  $\xi = -1$ ,  $\chi_a = 0.1$ ,  $\chi_m = 1$ ,  $\gamma = 10$ ,  $\nu = 1$ ,  $\rho_a^* = 5$  and  $\rho_a^h = 5$ . See Sec. 7 for details.



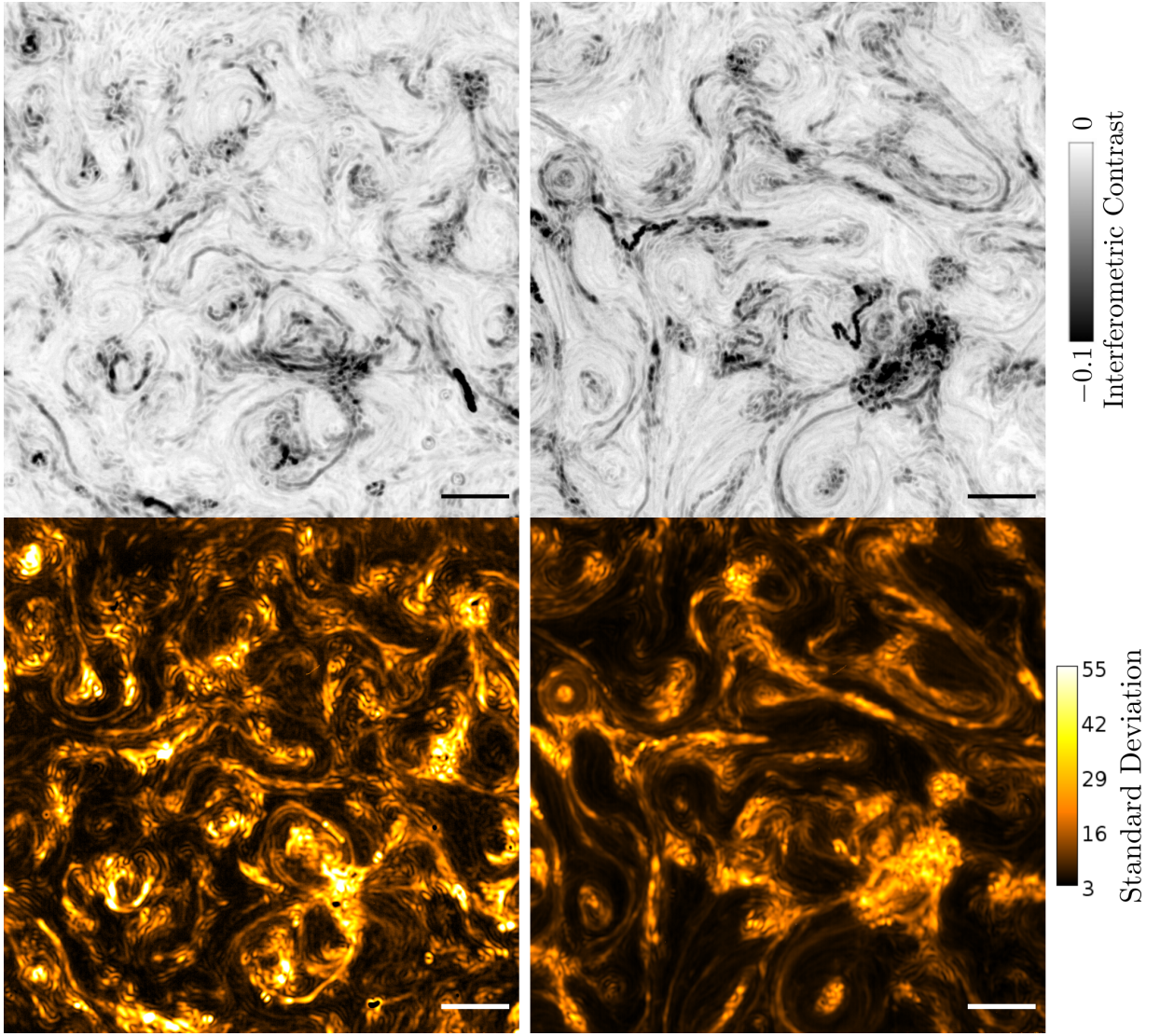


FIG. S5. Wideviews of the vortex regions in iSCAT, minimal intensity projections of differential images over a period of 120s above and the corresponding standard deviation below; scale bar  $5 \mu\text{m}$ , experimental conditions  $[\text{actin}] = 300\text{nM}$ ,  $[\text{myosin-II}] = 80\text{nM}$ ,  $\text{Length}(\text{F-actin}) = 7 \pm 3.5 \mu\text{m}$ .

### 3. Microscopic Model

Here, we include the details of the calculations for our microscopic model for the statistics of the bound status of the individual head groups belonging to a single myosin II minifilament (see Fig. 2 of main text).

a. Master Equations

In our model, the time-dependent probabilities  $P_n(t)$  for a single myosin II minifilament to have  $n$  headgroups bound are given by the following coupled, linear ODEs:

$$\frac{dP_0(t)}{dt} = k_{\text{off}}P_1(t), \quad (\text{S1})$$

$$\frac{dP_1(t)}{dt} = 2k_{\text{off}}P_2(t) - (N-1)k_{\text{on}}P_1(t) - k_{\text{off}}P_1(t), \quad (\text{S2})$$

$$\frac{dP_n(t)}{dt} = (N-n+1)k_{\text{on}}P_{n-1}(t) + (n+1)k_{\text{off}}P_{n+1}(t) - [(N-n)k_{\text{on}} + nk_{\text{off}}]P_n(t), \quad \forall n \in [2, N-1], \quad (\text{S3})$$

$$\frac{dP_N(t)}{dt} = k_{\text{on}}P_{N-1}(t) - Nk_{\text{off}}P_N(t), \quad (\text{S4})$$

with initial condition  $P_1(0) = 1$  (*i.e.*, one headgroup bound) representing an the first state of the minifilament on binding from the bulk. We are interested in the average dwell time of the myosin filament on the actin filament, or the mean first passage time into the  $n = 0$  state (*i.e.* dissociation from actin back to the bulk).

b. Recursive solution for mean first passage time starting from one headgroup bound

The distribution of such first passage times to dissociation is given by

$$f_0(T) = \Pr \{x(T) = 0, x(t) \neq 0 \forall 0 \leq t < T \mid x(0) = 1\}, \quad (\text{S5})$$

with mean

$$\langle T_0 \rangle = \int_0^\infty t f_0(t) dt = -\partial_s [\bar{f}_0(s)]|_{s=0}, \quad (\text{S6})$$

where  $\bar{f}_0(s)$  denotes the Laplace transform of  $f_0(t)$ . Taking the Laplace transform of the master equations (S4) gives

$$s\bar{P}_0 = k_{\text{off}}\bar{P}_1, \quad (\text{S7})$$

$$s\bar{P}_1 - 1 = 2k_{\text{off}}\bar{P}_2 - (N-1)k_{\text{on}}\bar{P}_1 - k_{\text{off}}\bar{P}_1, \quad (\text{S8})$$

$$s\bar{P}_n = (N-n+1)k_{\text{on}}\bar{P}_{n-1} + (n+1)k_{\text{off}}\bar{P}_{n+1} - [(N-n)k_{\text{on}} + nk_{\text{off}}]\bar{P}_n, \quad \forall n \in [2, N-1], \quad (\text{S9})$$

$$s\bar{P}_N = k_{\text{on}}\bar{P}_{N-1} - Nk_{\text{off}}\bar{P}_N, \quad (\text{S10})$$

which can be solved recursively to give

$$\frac{\bar{P}_n}{\bar{P}_{n-1}} = \frac{(N-n+1)k_{\text{on}}}{s + (N-n)k_{\text{on}} + nk_{\text{off}} - (n+1)k_{\text{off}}\frac{\bar{P}_{n+1}}{\bar{P}_n}}, \quad \forall n \in [2, N], \quad (\text{S11})$$

$$\bar{P}_1 = \frac{1}{s + (N-1)k_{\text{on}} + k_{\text{off}} - 2k_{\text{off}}\frac{\bar{P}_2}{\bar{P}_1}}, \quad (\text{S12})$$

$$s\bar{P}_0 = k_{\text{off}}\bar{P}_1 = \frac{k_{\text{off}}}{s + (N-1)k_{\text{on}} + k_{\text{off}} - 2k_{\text{off}}\frac{\bar{P}_2}{\bar{P}_1}}, \quad (\text{S13})$$

with termination condition  $\bar{P}_{N+1} = 0$ .

The mean first passage, or equivalently, mean residence times,  $\langle T_0 \rangle$ , for  $N \in [1, 5]$  are plotted in Fig. S6 as a function of the ratio of off- to on-rates,  $k_{\text{off}}/k_{\text{on}}$ . In the limit of large  $k_{\text{on}}$ , the dwell time scales like  $\langle T_0 \rangle \sim k_{\text{on}}^{N-1}$ , whereas for large  $k_{\text{off}}$ , we have  $\langle T_0 \rangle \sim k_{\text{off}}^{-1}$ . The functional form of the dwell times for  $N \in [1, 5]$  are given by:

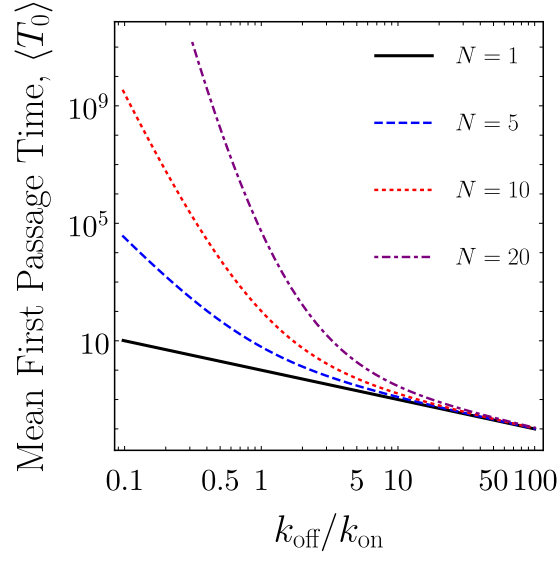


FIG. S6. Mean first passage time,  $\langle T_0 \rangle$ , for a single myosin II mini-filament with  $N$  headgroups to dissociate after starting with one headgroup bound. Plotted as a function of the ratio of headgroup off- to on- rates,  $k_{\text{off}}/k_{\text{on}}$ , in units of  $k_{\text{on}}^{-1}$ .

$$\begin{aligned}
 N = 1: \quad \langle T_0 \rangle &= \frac{1}{k_{\text{off}}}, \\
 N = 2: \quad \langle T_0 \rangle &= \frac{2k_{\text{off}} + k_{\text{on}}}{2k_{\text{off}}^2}, \\
 N = 3: \quad \langle T_0 \rangle &= \frac{3k_{\text{off}}^2 + 3k_{\text{off}}k_{\text{on}} + k_{\text{on}}^2}{3k_{\text{off}}^3}, \\
 N = 4: \quad \langle T_0 \rangle &= \frac{(2k_{\text{off}} + k_{\text{on}})(2k_{\text{off}}^2 + 2k_{\text{off}}k_{\text{on}} + k_{\text{on}}^2)}{4k_{\text{off}}^4}, \\
 N = 5: \quad \langle T_0 \rangle &= \frac{5k_{\text{off}}^4 + 10k_{\text{off}}^3k_{\text{on}} + 10k_{\text{off}}^2k_{\text{on}}^2 + 5k_{\text{off}}k_{\text{on}}^3 + k_{\text{on}}^4}{5k_{\text{off}}^5}.
 \end{aligned}$$

### c. Sum-over paths representation

Here we outline a sum-over-paths approach, which is an alternate method of calculating the mean first passage time that also permits the computation of the mean number of visits to each state in our microscopic model [68].

Consider a sequence of jumps on the ladder state-space that represents number of bound headgroups of a single myosin II minifilament (see Fig. 2a in main text) beginning with one headgroup attached and terminating when the filament drops off (*i.e.*, 0 headgroups bound). The probability of realising this sequence of jumps is given by the sum over the probabilities of all such trajectories

$$\Pr(\mathcal{S} = (1, \dots, 0)) = \int_{t_0 < \dots < t_n} \left( \prod_{i=0}^n dt_i \right) \Pr(\mathcal{T} = ((1, t_0), \dots, (0, t_n))), \quad (\text{S14})$$

where the probability of a given trajectory is just given by the product of the transition probabilities making up that trajectory

$$\Pr(\mathcal{T} = ((1, t_0), \dots, (0, t_n))) = \prod_{i=0}^{n-1} Q_{i \rightarrow j}(t_{i+1} - t_i). \quad (\text{S15})$$

The transition probabilities are themselves given by the product of the waiting time distributions,  $P_{i \rightarrow j}(t)$ , and survivor functions,  $S_{i \rightarrow k}(t)$ :

$$Q_{i \rightarrow j}(t) = P_{i \rightarrow j}(t) \prod_{k \neq i, j} S_{i \rightarrow k}(t), \quad (\text{S16})$$

where  $S_{i \rightarrow k}(t) = 1 - \int_0^t P_{i \rightarrow k}(\tau) d\tau$ . In general, the waiting time distributions are exponential (*i.e.*, Poissonian) with a form  $P_{i \rightarrow j}(t) = \lambda_{i \rightarrow j} \exp(-\lambda_{i \rightarrow j} t)$ , where the rates  $\lambda_{i \rightarrow j}$  can be read off the master equation, Eqs. (S1–S4). By making use of the convolution properties of the Laplace transform we see

$$\Pr(\mathcal{S} = (1, \dots, 0)) = \prod_{i=0}^{n-1} \bar{Q}_{i \rightarrow j}(0), \quad (\text{S17})$$

where the bar denotes the Laplace transform. From this, we define a matrix  $\mathbf{A}$  with coefficients,

$$A_{ij} = \bar{Q}_{i \rightarrow j}(s). \quad (\text{S18})$$

Raising  $\mathbf{A}$  to the power  $n$  and taking the  $i0$  component (*i.e.*,  $[\mathbf{A}^n]_{i0}$ ) is then just the Laplace transform of the distribution of first passage times into the absorbing state, 0, in  $n$  steps, starting from initial state  $i$ . Thus, taking  $i = 1$ , summing over all possible paths and taking the Neumann sum we find

$$\bar{f}_0(s) = \left[ \sum_{n=0}^{\infty} \mathbf{A}^n \right]_{i0} = \left[ (\mathbb{I} - \mathbf{A})^{-1} \right]_{i0}, \quad (\text{S19})$$

from which  $\langle T_0 \rangle$  can be readily calculated [see Eq. (S6)]. To calculate the average number of times a particular transition happens,  $\#(i \rightarrow j)$ , we define the matrix  $\mathbf{B}$ , with coefficients

$$B_{kl}(z) = \begin{cases} z A_{kl}(0) & \forall (k, l) = (i, j) \\ A_{kl}(0) & \text{otherwise} \end{cases}, \quad (\text{S20})$$

so that the corresponding Neumann series gives the generating function of the probability distribution of a sequence where  $\#(i \rightarrow j) = m$ —*i.e.*, some sequence, starting with 1 headgroup bound and ending in dissociation, where the transition  $i \rightarrow j$  occurs  $m$  times:

$$G(z) = \sum_{m=0}^{\infty} z^m P(m) = \left[ \sum_{n=0}^{\infty} \mathbf{B}^n \right]_{10} = \left[ (\mathbb{I} - \mathbf{B})^{-1} \right]_{10}. \quad (\text{S21})$$

As a result, it follows that

$$\langle \#(i \rightarrow j) \rangle = \langle m \rangle = \partial_z G(z)|_{z \rightarrow 1}. \quad (\text{S22})$$

To illustrate via a concrete example, consider the case of 5 headgroups, for which we have

$$\mathbf{A}(s) = \begin{pmatrix} 0 & 0 & 0 & 0 & 0 & 0 \\ \frac{k_{\text{off}}}{k_{\text{off}} + 4k_{\text{on}} + s} & 0 & \frac{4k_{\text{on}}}{k_{\text{off}} + 4k_{\text{on}} + s} & 0 & 0 & 0 \\ 0 & \frac{2k_{\text{off}}}{2k_{\text{off}} + 3k_{\text{on}} + s} & 0 & \frac{3k_{\text{on}}}{2k_{\text{off}} + 3k_{\text{on}} + s} & 0 & 0 \\ 0 & 0 & \frac{3k_{\text{off}}}{3k_{\text{off}} + 2k_{\text{on}} + s} & 0 & \frac{2k_{\text{on}}}{3k_{\text{off}} + 2k_{\text{on}} + s} & 0 \\ 0 & 0 & 0 & \frac{4k_{\text{off}}}{4k_{\text{off}} + k_{\text{on}} + s} & 0 & \frac{k_{\text{on}}}{4k_{\text{off}} + k_{\text{on}} + s} \\ 0 & 0 & 0 & 0 & \frac{5k_{\text{off}}}{5k_{\text{off}} + s} & 0 \end{pmatrix}, \quad (\text{S23})$$

which implies a mean first passage time to dissociation of the form

$$\langle T_0 \rangle = \frac{5k_{\text{off}}^4 + 10k_{\text{off}}^3 k_{\text{on}} + 10k_{\text{off}}^2 k_{\text{on}}^2 + 5k_{\text{off}} k_{\text{on}}^3 + k_{\text{on}}^4}{5k_{\text{off}}^5}. \quad (\text{S24})$$

Using the same example, but picking out the transition  $1 \rightarrow 2$ , we write

$$\mathbf{B}(s) = \begin{pmatrix} 0 & 0 & 0 & 0 & 0 & 0 \\ \frac{k_{\text{off}}}{k_{\text{off}} + 4k_{\text{on}} + s} & 0 & \frac{4k_{\text{on}} z}{k_{\text{off}} + 4k_{\text{on}} + s} & 0 & 0 & 0 \\ 0 & \frac{2k_{\text{off}}}{2k_{\text{off}} + 3k_{\text{on}} + s} & 0 & \frac{3k_{\text{on}}}{2k_{\text{off}} + 3k_{\text{on}} + s} & 0 & 0 \\ 0 & 0 & \frac{3k_{\text{off}}}{3k_{\text{off}} + 2k_{\text{on}} + s} & 0 & \frac{2k_{\text{on}}}{3k_{\text{off}} + 2k_{\text{on}} + s} & 0 \\ 0 & 0 & 0 & \frac{4k_{\text{off}}}{4k_{\text{off}} + k_{\text{on}} + s} & 0 & \frac{k_{\text{on}}}{4k_{\text{off}} + k_{\text{on}} + s} \\ 0 & 0 & 0 & 0 & \frac{5k_{\text{off}}}{5k_{\text{off}} + s} & 0 \end{pmatrix}, \quad (\text{S25})$$

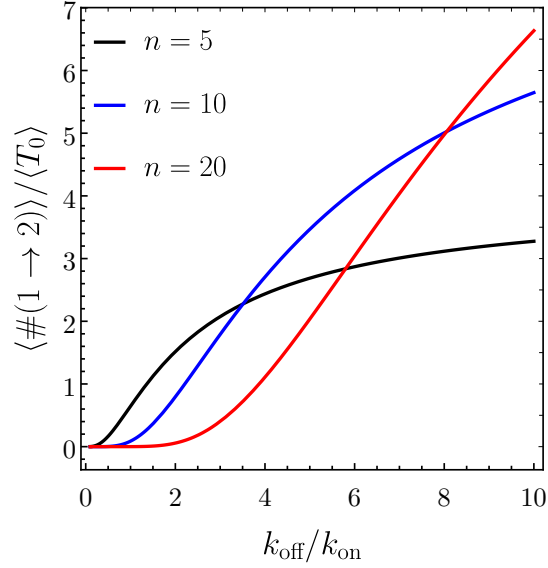


FIG. S7. Average number of times a transition from two heads to one head bound occurs, divided by mean first passage time (*i.e.*,  $\langle \#(1 \rightarrow 2) \rangle / \langle T_0 \rangle$ ) plotted against  $k_{\text{off}}/k_{\text{on}}$  for different total number of headgroups on the myosin II minifilament,  $n$ . We identify this transition with a processive-like power stroke due to the lack of crosslinking.

and therefore

$$\langle \#1 \rightarrow 2 \rangle = \frac{4k_{\text{on}}}{k_{\text{off}}}. \quad (\text{S26})$$

Under the assumption that every transition between states of increasing number— *i.e.*,  $i \rightarrow i + 1$  *etc.*— involves a single “powerstroke”, we can further categorise such transitions and therefore their rates. For example, we identify the transition  $1 \rightarrow 2$  with processive motion; when myosin II minifilaments take a step along actin. In this case, the ratio  $\langle \#(1 \rightarrow 2) \rangle / \langle T_0 \rangle$  quantifies the rate at which a single minifilament makes processive steps on average. This is plotted for differing numbers of heads and  $k_{\text{off}}/k_{\text{on}}$  in Fig. S7. A histogram of such average rates, over all transitions, can also be plotted (see Fig. S8 for  $N = 10$ ). This shows that, as the off-rate is increased, the filament spends more of its time in the states with only a few heads bound and therefore has an increased likelihood of processive motion (note, uninterrupted walking corresponds to the sequence:  $1 \rightarrow 2 \rightarrow 1 \rightarrow 2 \dots$  *etc.*).

If *more* than 2 head groups are bound, we assume one of two scenarios. Either, the additional bindings stall any attempted procession along actin, or, the head groups are bound across more than one actin filament, and the powerstroke results in relative motion of two or more filaments, *i.e.* contractility. Summing the number of “up” transitions per mean first passage time for each regime gives a processivity and contractility respectively which are plotted in Fig. S9. For large  $k_{\text{off}}/k_{\text{on}}$  the processive rate is approximately constant and the contractility scales like  $k_{\text{on}}/k_{\text{off}}$ , we will make use of this crude scaling in our hydrodynamic model and use it to gain some insight into the ATP dependence of structures seen in experiment.

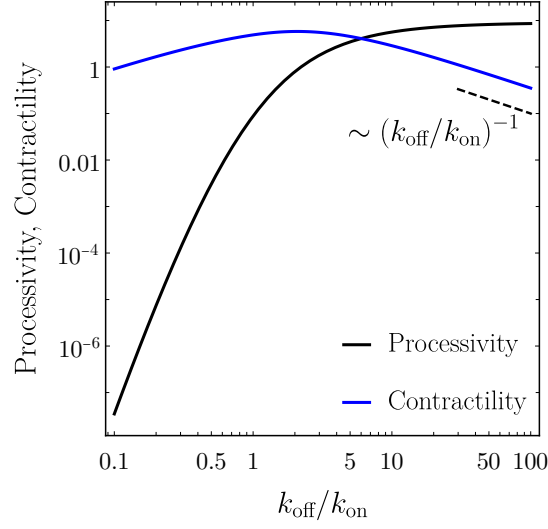
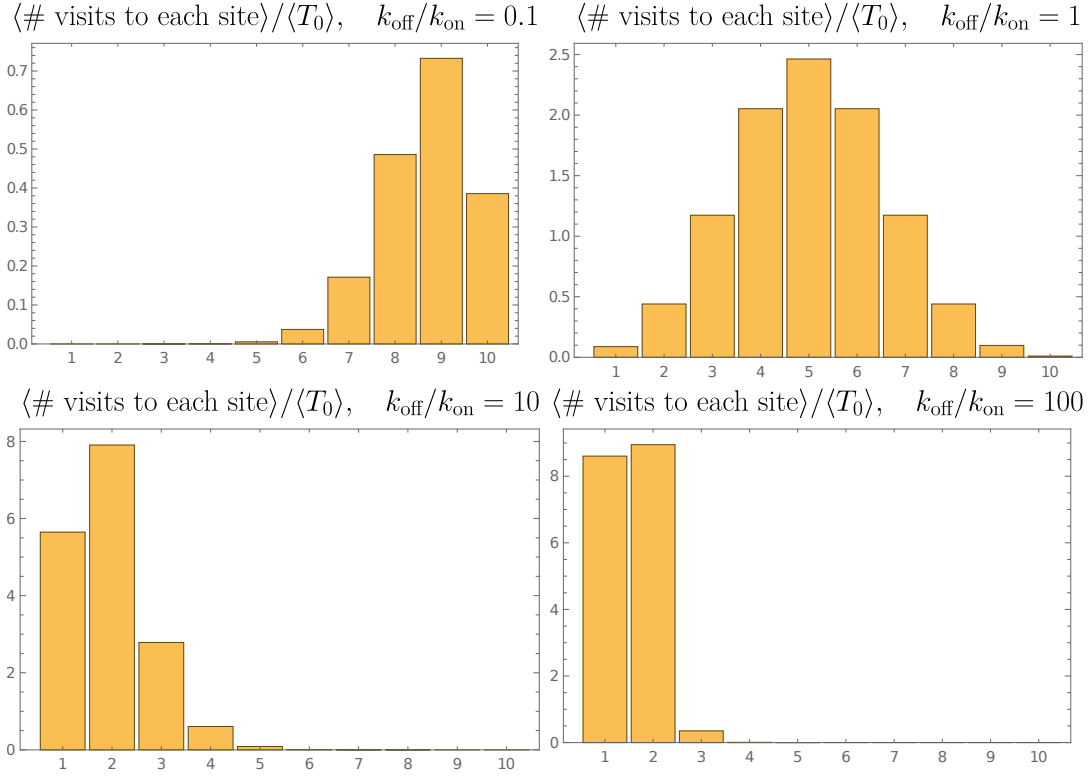
#### 4. Hydrodynamic Model

Here we present the details and solutions to the hydrodynamic model presented in the main text. We take a typical active hydrodynamics approach for a polar gel. This comprises conservation equations for both myosin and actin densities, force balance conditions that apply between the SLB and actin, and actin and myosin, and a dynamical equation for the broken symmetry field representing the local average of the direction (towards the plus end) of the the actin at each point [2, 4, 26, 30–32].

##### a. Derivation of dynamical equations

We assume that the system can be modelled as a triple layered system of myosin-II mini-filaments atop actin, which in turn is crosslinked *via* ezrin to a supported lipid bilayer (SLB). We will treat the SLB as a momentum sink such





that it only enters the equations for actin via a friction term and does not require the solving of the 2D Stokes (or D'Arcy equations) in the presence of force point forces representing ezrin.

The actin density,  $\rho_a$ , and myosin density,  $\rho_m$ , obey continuity equations with source and sink terms for the latter representing the binding/unbinding of minifilaments from the bulk. These are given by

$$\partial_t \rho_a + \nabla_i J_a^i = 0, \quad (\text{S27})$$

$$\partial_t \rho_m + \nabla_i J_m^i = k_{\text{on}}^m \frac{\rho_a}{\rho_a + \rho_a^h} - k_{\text{off}}^m \rho_m / \phi, \quad (\text{S28})$$

where we have assumed a saturating Hill-form (with respect to actin density) for the myosin minifilament on-rate as well as an off-rate that is linear in myosin minifilament density. The actin and myosin currents are given by  $J_{m,a}^i = v_{m,a}^i \rho_{m,a}$  respectively, where  $v_{m,a}^i$  are the components of myosin and actin velocities.

Since the actin is characterised by a polarization (broken symmetry) field,  $\vec{P}$ , the total stress in the actin layer is given by the tensor  $\Sigma^{ij} = \sigma^{ij} + \frac{1}{2} (P^i h^j - h^i P^j)$ , where  $h^i$  is the molecular field. The molecular field is derived from from an elastic Frank free energy that we assume to be in the one-constant approximation:

$$\mathcal{F} = \int \frac{\kappa}{2} |\nabla_i P^j|^2 d^2x; \quad h^i = -\frac{\delta \mathcal{F}}{\delta P_i} = \kappa \Delta P^i \quad (\text{S29})$$

where  $\kappa$  is the elastic modulus and  $\Delta = \nabla_i \nabla^i$  is the Laplacian.

We assume a fluid like constitutive relation for the actin in the frictional limit, where the dominant dissipative term is friction with the membrane rather than intra-actin viscosity. The symmetric part of the actin stress tensor is therefore given by the following relation for an active ordered fluid

$$\sigma^{ij} = -\zeta(\vec{r}) g^{ij} - \bar{\zeta}(r) P^i P^j + (\chi_m \rho_m - \chi_a \rho_a) g^{ij}, \quad (\text{S30})$$

where  $\zeta$  and  $\bar{\zeta}$  are the active isotropic and anisotropic stresses, and  $g^{ij}$  is the inverse of the metric. Assuming that the friction between the myosin and actin layer is given by  $\Gamma_m = \beta_m \rho_m$  and between the actin and SLB by  $\Gamma_a = \beta_a \rho_a$ , the corresponding force balance conditions are then given by

$$\Gamma_m (v_m^i - v_a^i) = -\alpha v_0 \beta_m \rho_m P^i - \chi_m \nabla^i \rho_m, \quad (\text{S31})$$

and

$$\Gamma_a v_a^i + \Gamma_m (v_a^i - v_m^i) = \alpha v_0 \beta_m \rho_m P^i + \nabla_j \Sigma^{ij}, \quad (\text{S32})$$

respectively, where  $v_0$  is a characteristic rate of myosin procession along actin, and  $\alpha$  is a scalar that encodes the dependence of this velocity on non-hydrodynamic variables such as the concentration of ATP.

The objective rate for the polarization,  $P^i$ , is given by  $D_t P^i = \partial_t P^i + v_a^j \nabla_j P^i + \Omega^i_j P^j$ , where  $\Omega_{ij} = \frac{1}{2} (\nabla_i v_{aj} - \nabla_j v_{ai})$  is the vorticity. This appears in the dynamical equation for the polarization field, which is given by

$$D_t P^i = \frac{h^i}{\gamma} + \nu \left[ \frac{\rho_a}{\rho_a^*} (1 - P_j P^j) - (1 + P_j P^j) \right] P^i, \quad (\text{S33})$$

where the second term ensures  $|P| \rightarrow 1$  when  $\rho_a > \rho_a^*$ . When deep in the nematic phase, we can approximate this as

$$D_t P^i = \frac{h^i}{\gamma} + \lambda P^i, \quad (\text{S34})$$

where we introduce a Lagrange multiplier,  $\lambda$ , in order to impose  $|\vec{P}| = 1$ . Here we will also assume the actin is sufficiently dense that the on-rate of myosin motors saturates. This gives a simplified continuity equation of the following form

$$\partial_t \rho_m + \nabla_i J_m^i = k_{\text{on}}^m - k_{\text{off}}^m \rho_m / \phi. \quad (\text{S35})$$

#### *b. Steady-state equations in the axisymmetric case*

We will consider a simplified scenario for steady states where all variables are axisymmetric such that they depend only on the radial coordinate,  $r$ , and not on the polar angle,  $\theta$ . We assume that we are in the dense, nematic phase and look for solutions in steady state.

The polarization field we choose to be given by  $\vec{P} = \cos \psi(r) \vec{e}_r + \sin \psi(r) \vec{e}_\theta$  and we decompose the molecular field into parallel and perpendicular components

$$h_{\parallel} = h_r \cos \psi + h_\theta \sin \psi \quad (\text{S36})$$

$$h_{\perp} = -h_r \sin \psi + h_\theta \cos \psi \quad (\text{S37})$$

where  $h_r$  and  $h_\theta$  are the components of  $\vec{h}$  in polar coordinates. From the one-contant Frank free energy we find

$$h_\perp = \kappa \left[ \partial_r^2 \psi + \frac{\partial_r \psi}{r} \right]. \quad (\text{S38})$$

The continuity equations simplify to

$$k_{\text{off}} \rho_m / \bar{\phi} - k_{\text{on}} + \rho_m \partial_r v_m^r + v_m^r \partial_r \rho_m + \frac{\rho_m v_m^r}{r} = 0 \quad (\text{S39})$$

$$\rho_a \partial_r v_a^r + v_a^r \partial_r \rho_a + \frac{\rho_a v_a^r}{r} = 0. \quad (\text{S40})$$

The components of the actin stress tensor,  $\sigma$ , are given by the following

$$rr : \quad -\frac{1}{2} \{ \bar{\zeta} \cos(2\psi) + \bar{\zeta} + 2\zeta \} \quad (\text{S41})$$

$$\theta\theta : \quad \frac{1}{2} \{ \bar{\zeta} \cos(2\psi) - \bar{\zeta} - 2\zeta \} \quad (\text{S42})$$

$$r\theta : \quad -\frac{1}{2} \bar{\zeta} \sin(2\psi). \quad (\text{S43})$$

The polarization equation can be re-written as

$$\frac{h_\parallel}{\gamma} = 0 \quad (\text{S44})$$

$$-\frac{h_\perp}{\gamma} - \frac{1}{2} \partial_r v_a^\theta + \frac{v_a^\theta + 2r v_a^r \partial_r \psi}{2r} = 0 \quad (\text{S45})$$

The components of the myosin force balance equation are given by

$$\vec{e}_r : \quad \Gamma_m (v_m^r - v_a^r) = -\alpha \cos(\psi) - \chi_m \partial_r \rho_m \quad (\text{S46})$$

$$\vec{e}_\theta : \quad \Gamma_m (v_m^\theta - v_a^\theta) = -\alpha \sin(\psi) \quad (\text{S47})$$

where  $\alpha = v_0 \beta_m \rho_m$  and  $\Gamma_m = \beta_m \rho_m$ .

This tensor divergence has the following components in polar coordinates

$$\vec{e}_r : \quad \partial_r \Sigma_{rr} + \frac{1}{r} \partial_\theta \Sigma_{r\theta} + \frac{\Sigma_{rr} - \Sigma_{\theta\theta}}{r} \quad (\text{S48})$$

$$\vec{e}_\theta : \quad \partial_r \Sigma_{\theta r} + \frac{1}{r} \partial_\theta \Sigma_{\theta\theta} + \frac{\Sigma_{\theta r} + \Sigma_{r\theta}}{r} \quad (\text{S49})$$

and hence the actin force balance by

$$\begin{aligned} \vec{e}_r : \quad & \frac{1}{2r} \left\{ \cos(2\psi) \left[ r \left( \partial_r \bar{\zeta} \right) + 2\bar{\zeta} \right] + r \left( \partial_r \bar{\zeta} + 2\partial_r \zeta + 2\partial_r \Pi_a \right) - \sin(2\psi) \left( 2r \partial_r \psi \bar{\zeta} \right) \right\} \\ & - \Phi \cos(\psi) + \Gamma_a v_a^r + \Gamma_m (v_a^r - v_m^r) = 0 \end{aligned} \quad (\text{S50})$$

$$\begin{aligned} \vec{e}_\theta : \quad & \frac{1}{2r} \left\{ \sin(2\psi) \left[ r \partial_r \bar{\zeta} + 2\bar{\zeta} \right] + \cos(2\psi) \left( 2r \partial_r \psi \bar{\zeta} \right) - r \partial_r h_\perp \right\} \\ & - \Phi \sin(\psi) + \Gamma_a v_a^\theta + \Gamma_m (v_a^\theta - v_m^\theta) = 0 \end{aligned} \quad (\text{S51})$$

where  $\Pi_a = \chi_m \rho_m - \chi_a \rho_a$ ,  $\Phi = \alpha v_0 \beta_m \rho_m$ ,  $\Gamma_a = \beta_a \rho_a$  and  $\Gamma_m = \beta_m \rho_m$ .

### c. Non-dimensionalisation and scaling of the active stress

Taking the myosin continuity equation we can write it in dimensionless form as

$$\partial_t \rho_m + \vec{\nabla} \cdot (\rho_m \vec{v}_m) = \frac{k_{\text{on}}^{(0)} \tau}{\phi} [1 - k \rho_m] \quad (\text{S52})$$

where  $\tau$  is some characteristic time-scale and  $k = k_{\text{off}}/k_{\text{on}}$ . We will choose  $\tau = \phi/k_{\text{on}}$  as our characteristic time-scale as we expect the characteristic time to scale like the dwell time which goes like the inverse of  $k_{\text{off}}$  as ATP is varied, see Sec. 3. We have assumed  $\phi$  is the characteristic density scale. The characteristic time-scales and length-scales are given by

$$\tau = \frac{\phi}{k_{\text{on}}}; \quad L = v_0 \tau \quad (\text{S53})$$

where  $v_0$  is the active precession velocity of myosin. The dimensionless equation for myosin density then becomes

$$\partial_t \rho_m + \vec{\nabla} \cdot (\rho_m \vec{v}_m) = 1 - k \rho_m. \quad (\text{S54})$$

From this we can proceed to non-dimensionalise the equations of motion where now all the coefficients are dimensionless as follows  $\chi_m \phi / (L \beta_m) \rightarrow \chi_m$ ,  $\chi_a \phi / (L \beta_a) \rightarrow \chi_a$ ,  $\xi \tau / \beta_a \phi L \rightarrow \xi$  and  $\tau / \gamma \rightarrow 1 / \gamma$ . This gives the equations quoted in the main text, Eqs. (1-6). We will also assume that  $\chi_a \sim 1/k$  in terms of magnitude.

The active parameter in our model have been chosen to be of the following form

$$\zeta = \frac{\rho_m}{k} \xi; \quad \bar{\zeta} = \frac{\rho_m}{k} \bar{\xi} \quad (\text{S55})$$

where we will label the prefactor in the high ATP regime (large  $k$ ) as  $1/k = \epsilon$ . This form gives the correct scaling in terms of  $k_{\text{off}}$  in the limit of low myosin density.

#### d. Neglecting anisotropic active stress

Here we will briefly justify our reasons for neglecting the anisotropic active part of the stress tensor in further analysis and in the main text. The anisotropic term is of the form

$$\sigma_{pp} = \bar{\zeta} \vec{P} \vec{P} \quad (\text{S56})$$

depending on the sign of this term it can either stabilise or destabilise bend and splay respectively, see Fig. S10L. This term would not only lead to an expulsion of actin from the centre of the aster (discussed in detail later), Fig. S10R, but also to excessive shear banding not seen in experiments. For these reason we will choose to neglect it from our analysis as it does not seem to play a large role in the system. Similar approaches in the literature also make this approximation, see, for example, [31].

#### e. Quasi-steady state equations for higher ATP concentrations: perturbative solution

Here we outline the quasi steady state multi-timescale expansion which we will use to find solutions for the spiral texture (we solve the full equations in the case of the aster as they are genuine steady-state solutions at low ATP).

For low myosin density and high ATP concentration  $\epsilon = \rho_m / k \rho_a$  is then a small parameter. Assuming the non-dimensionalised actin diffusion is of a similar order of magnitude to  $\epsilon$  and adding the equations for myosin and actin force balance together gives

$$\vec{v}_a = \nabla \cdot \Sigma - \chi_a \nabla \rho_a \sim \mathcal{O}(\epsilon). \quad (\text{S57})$$

All the terms in the stress tensor are of linear order in  $\epsilon$  and  $\kappa$  (as they all pre-multiply terms which go like either the shear rate  $u \sim \epsilon$  or  $\vec{h} \sim \kappa$  and are thus quadratic in order).

The zeroth order equation for myosin force balance and first order for actin force balance are then given by

$$\vec{v}_m = -\vec{P} - \frac{\chi_m}{\rho_m} \nabla \rho_m + \mathcal{O}(\epsilon) \quad (\text{S58})$$

$$\vec{v}_a = -\left[ \frac{1}{\rho_a} \nabla \cdot \left\{ \zeta(\rho_m, \rho_a) \mathbb{I} - \frac{1}{2} \left( \vec{P} \vec{h} - \vec{h} \vec{P} \right) \right\} + \frac{\chi_a}{\rho_a} \nabla \rho_a \right] + \mathcal{O}(\epsilon^2). \quad (\text{S59})$$

This system can then be solved hierarchically with solutions which go like

$$f(x) = \sum_n f^{(n)}(x) \text{ where } f^{(n)} \sim \mathcal{O}(\epsilon^r \kappa^s) \text{ and } r + s = n \quad (\text{S60})$$

where we pick can pick a texture and initial actin density solve independently for the myosin velocity and density and use this to compute the actin velocity, and thus how the underlying texture remodels. Even at this level we can already see that this simple expansion gives an experimentally observable prediction in that the actin velocity at plentiful ATP will be much slower than the myosin velocity.

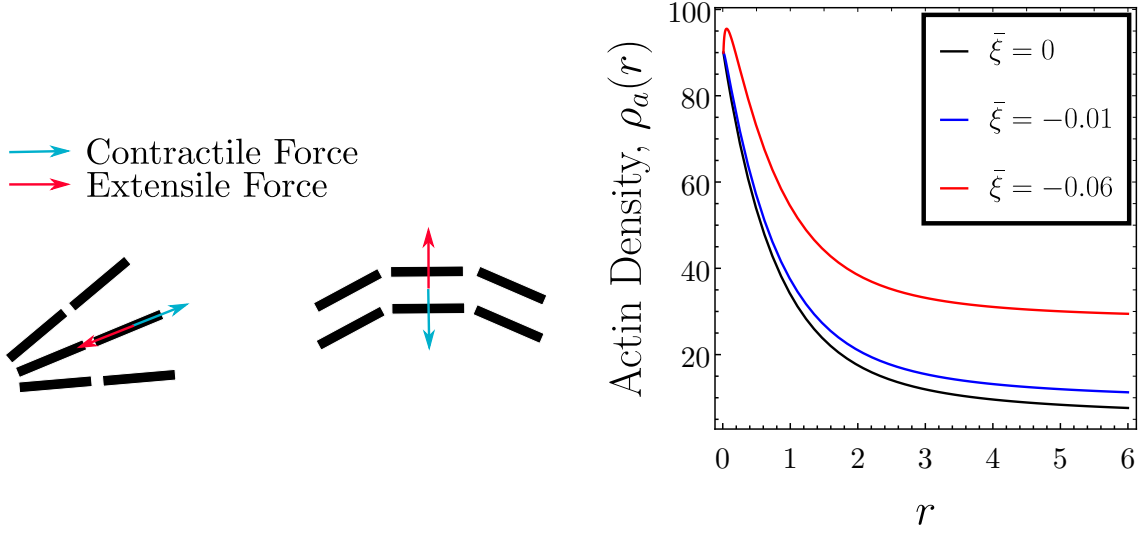


FIG. S10. **Left:** figure showing the active forcing to both splay and bend from a  $\sim \bar{\zeta} \bar{P} \bar{P}$  term in the contractile  $\bar{\zeta} < 0$  and extensile  $\bar{\zeta} > 0$  case. **Right:** Actin density in the case of the aster texture for different values of anisotropic active stress where  $\bar{\zeta} = \frac{\bar{\xi} \rho_m}{k}$ .

## 5. Numerical solution to the steady state equations

Here we discuss the numerical solutions in the case of the “aster” and “spiral” textures.

### a. Aster/contractile foci texture

For the regime with mostly depleted ATP we consider an aster texture as the possible steady state. An axisymmetric steady state texture of the following form is chosen

$$\vec{P} = \vec{e}_r; \quad \psi = 0. \quad (\text{S61})$$

This give  $\vec{h} = 0$  as the texture has no bend and actin velocities are also zero by symmetry arguments, conservation of actin mass and a little algebra.<sup>1</sup>

The force balance equations for myosin (in the absence of actin flows, which are zero for the aster texture) now reduce to the following equations for the myosin velocity

$$v_m^r = -\frac{\chi_m \partial_r \rho_m}{\rho_m} - 1; \quad v_m^\theta = 0. \quad (\text{S62})$$

This implies that  $\vec{v}_m$  is a function of  $\rho_m$ , such that the accumulation of myosin-II mini-filaments due to their procession towards texture’s centre is balanced by the density dependent dissociation rate.

This can be shown more directly by substituting into the continuity equation for myosin to give

$$\frac{\chi_m r \partial_r^2 \rho_m + (\chi_m + r) \partial_r \rho_m + (1 - kr) \rho_m + r}{r} = 0 \quad (\text{S63})$$

which is a boundary value problem for  $\rho_m(r)$  with boundary conditions of no flux at the origin and no gradients at infinity

$$\rho_m(0) = -\chi_m \partial_r \rho_m|_{r=0}; \quad \partial_r \rho_m|_{r \rightarrow \infty} = 0. \quad (\text{S64})$$

<sup>1</sup> We can argue that on physical grounds the aster is stable as the anisotropic active forcing or elastic splay forcing needed to destabilise them are not present in our model. The fact that we

see such stable structures in experiment is further justification for neglecting these terms.



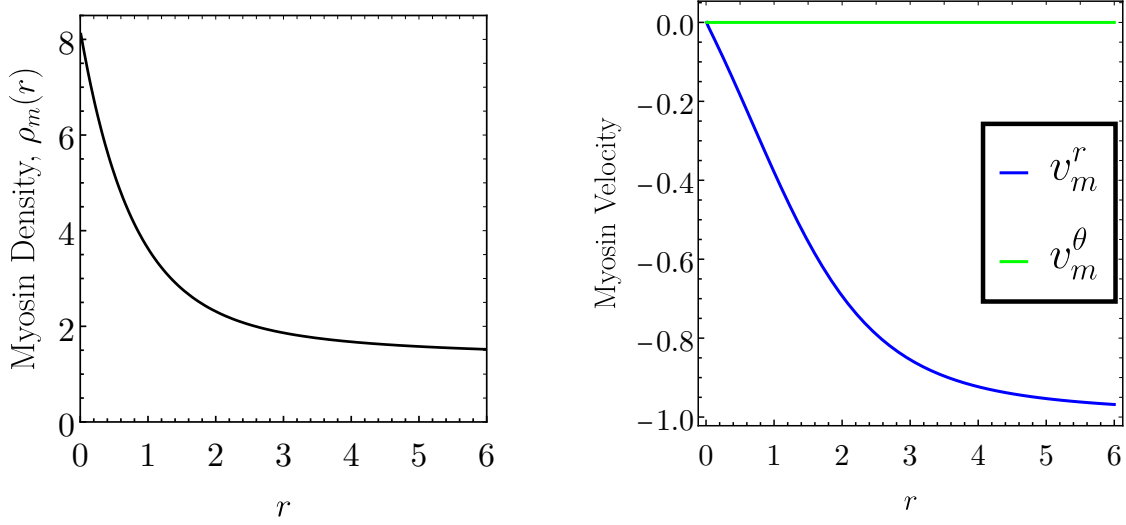


FIG. S11. Plots showing myosin density and velocity in the case of the aster texture for  $\chi_m = 1$ ,  $\chi_a = 0.1$ ,  $\xi = -1$  and  $k = 0.8$ .

Neither of these boundary conditions can be implemented exactly in a numerical scheme, so we choose to apply the first boundary condition at a small but finite radius choosing a value of  $\rho_m(0)$  which we then use as a shooting parameter to find a solution which is converging to flat in the far field. The numerical solutions to this are plotted in Fig. S11L where we choose  $\chi_m = 1$ ,  $\chi_a = 0.01$ ,  $\xi = -1$  and  $k = 1$  (also plotted in main text, see Fig. 3b). In this case we implement the center boundary condition at  $r=0.01$  and the final shooting value is chosen as  $\rho_m(0.01) = 8.1082$ . The corresponding myosin velocity field components are plotted in Fig. S11R.

With this solution we can now proceed to find the actin density by substituting into the remaining force balance condition for actin, which equates contractile forces with those resisting the compression of actin. This gives the following first order equation for  $\rho_a$  that is readily solvable numerically

$$\frac{\chi_a k r \partial_r \rho_a + r(\bar{\xi} + \xi) \partial_r \rho_m + \bar{\xi} \rho_m}{k r} = 0. \quad (\text{S65})$$

Here we keep the most general form, including anisotropic terms. In the main paper we set these to zero. We solve this for a boundary condition at  $r = 0.01$  that matches approximately with the actin and myosin density ratios seen in experiment ( $\sim 10 : 1$ ). In this case we choose  $\rho_m(0.01) = 15$ . The solutions to this are plotted in Fig. S12 with  $\bar{\xi} = 0$  for reasons stated in Sec. S4d (this is the equation used to plot Fig. S10R). Since it is qualitatively independent of  $k$ , we expect that the system converges to this state as ATP depletes, which is born out by the aster-like contractile foci seen in experiments (see Fig. 3a in main text).

#### b. Spiral/vortex texture

We now turn our attention to the quasi-steady state solutions that have a spiral/vortex-like character. In order to explain the long-lived vortex / spiral motifs of our experiments, we must take a perturbative approach: expanding in small  $\epsilon$  (high ATP) and solving hierarchically. At zeroth order,  $\vec{v}_a^{(0)} = 0$ , implying freedom to impose  $\vec{P}^{(0)}$  and  $\rho_a^{(0)}$ . We pick the following texture for the spiral in order to mimic the actin seen in TIRF and the flow dynamics of the myosin seen in iSCAT

$$\vec{P} = \frac{1}{\sqrt{\left(\frac{a^3 r^5}{(r+R)^3}\right)^2 + r^2 (R^2 - r^2)^4}} \left( r (R^2 - r^2)^2 \vec{e}_r + \frac{a^3 r^5}{(r+R)^3} \vec{e}_\theta \right) \quad (\text{S66})$$

this has a ring/vortex at  $r = R$  and then spirals inwards to a spiral-like focus at  $r = 0$ . This texture is plotted as an inset in the main text, Main Text Fig. 3f. We also choose actin density profile  $\rho_a^{(0)} = c r^2 e^{-r^2/w} + l$  with parameters to mimic a peak in actin density at the ring (as seen in TIRF data).

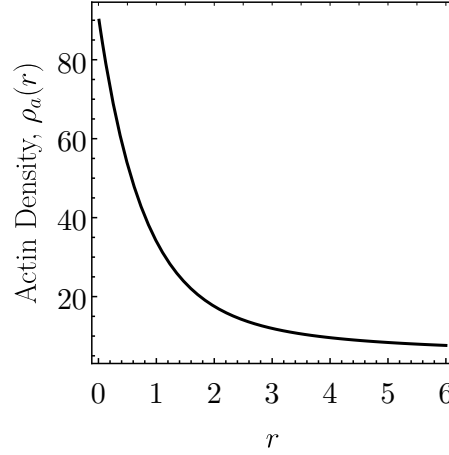


FIG. S12. Plots showing actin density in the case of the aster texture for  $\chi_m = 1$ ,  $\chi_a = 0.1$ ,  $\xi = -1$  and  $k = 0.8$ .

Making use of the multi-timescale expansion which is valid at higher ATP concentrations where these structures are seen simplifies the equations considerably and means we can solve the myosin flows on a fixed actin texture before computing the first order corrections to the actin flow later. The myosin mass conservation equation is given by

$$k - 1 + \rho_m \partial_r v_m^r + v_m^r \left( \partial_r \rho_m + \frac{\rho_m}{r} \right) = 0 \quad (\text{S67})$$

and the myosin force balance by

$$\vec{e}_r : \quad \chi_m \partial_r \rho_m + \rho_m v_m^r + \frac{\rho_m (r^2 - R^2)^2}{\sqrt{\frac{a^6 r^8}{(r+R)^6} + (r^2 - R^2)^4}} = 0 \quad (\text{S68})$$

$$\vec{e}_\theta : \quad \rho_m v_m^\theta + \frac{\rho_m a^3 r^4}{(r+R)^3 \sqrt{\frac{a^6 r^8}{(r+R)^6} + (r^2 - R^2)^4}} = 0. \quad (\text{S69})$$

In this case, the mini-filament velocity profile,  $\vec{v}_m$  is that which balances propulsive forces with density gradients.

Rearranging and substituting these expressions for the myosin velocity in terms of the myosin density into the continuity equations (Eq. S67) this can be solved using the same shooting method as in the aster case, as to lowest order in  $\epsilon$  these equations are completely decoupled from the actin dynamics. The boundary conditions are even identical. Solving this for  $\chi_m = 1$ ,  $R = 6$ ,  $a = 6$  and  $k = 10$  with shooting value  $\rho_m(0.01) = 0.412335913585$  gives the solutions plotted in Fig. S13. The results are in-line with experimental observations, with an inward flux of mini-filaments giving way to a circular motion around a central foci, at which point the high densities are balanced by high dissociation rates.

#### *First order corrections to the actin velocity*

As might be expected, this state is unstable at first order in  $\epsilon$ . We can, nevertheless, calculate first order corrections to the actin velocity profile,  $\vec{v}_a^{(1)}$ . As stated earlier we choose an initial actin density peaked about the ring (in imitation of the densities seen in TIRF experiments), hence we choose a ground state density of the the following form (for the parameters used to numerically solve the myosin dynamics previously)

$$\rho_a(r) = 0.1 r^2 e^{-r^2/36} + 1. \quad (\text{S70})$$

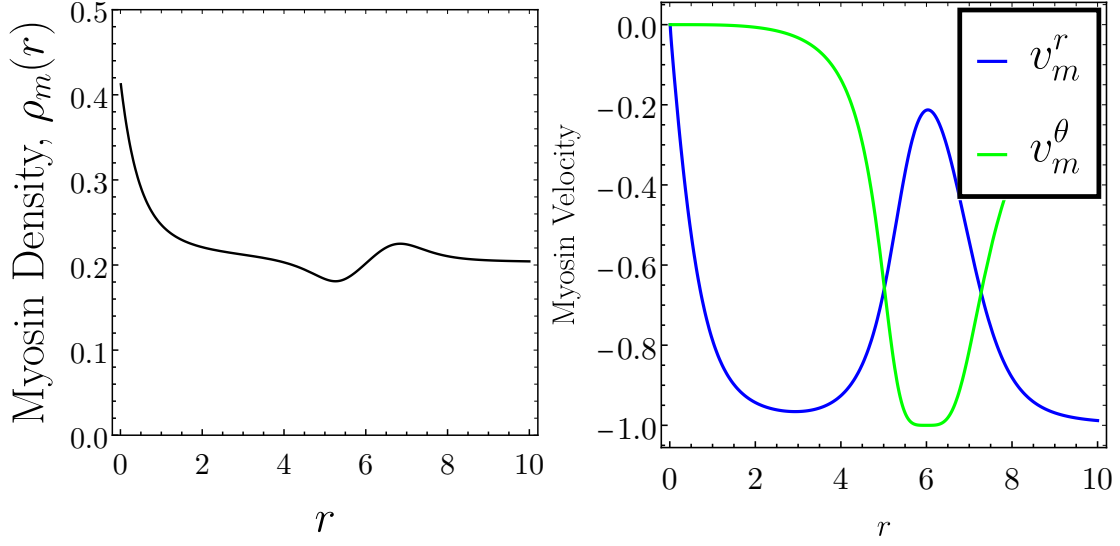


FIG. S13. Plots showing myosin density and velocity components in the case of the spiral texture for  $\chi_m = 1$ ,  $\chi_a = 0.1$ ,  $R = 6$ ,  $a = 6$ ,  $\kappa = 0.1$ ,  $\xi = -1$  and  $k = 10$ .

The actin force balance equation then reads

$$\vec{e}_r : \frac{-\chi_a k \partial_r \rho_a - \xi \partial_r \rho_m}{k \rho_a} = v_a^r \quad (\text{S71})$$

$$\begin{aligned} \vec{e}_\theta : & - \frac{a^3 \kappa r}{2 \rho_a(r) (a^6 r^8 + (r - R)^4 (r + R)^{10})^3} \left[ a^{12} r^{16} (9r^5 - 18r^4 R + 26r^3 R^2 - 34r^2 R^3 + 57r R^4 - 96R^5) (r + R)^2 \right. \\ & - 2a^6 r^8 (r - R)^3 (81r^6 - 234r^5 R + 511r^4 R^2 - 711r^3 R^3 + 756r^2 R^4 - 435r R^5 + 192R^6) (r + R)^{12} \\ & \left. + (r - R)^7 (45r^6 - 153r^5 R + 446r^4 R^2 - 462r^3 R^3 + 413r^2 R^4 - 129r R^5 + 32R^6) (r + R)^{22} \right] = v_a^\theta \end{aligned} \quad (\text{S72})$$

which gives the actin velocity  $\vec{v}_a^{(1)}$ . This, along with the initial actin density, are plotted in Fig. S14. In addition to radial corrections, this results in a small circular flow in the same direction as the myosin-II minifilaments that is accompanied by a slight shear-banding. The former is consistent with our observations, whilst the latter is either not present, or cannot be observed.

## 6. Linear Stability Analysis

Here we perform a linear stability analysis around an ordered uniform state to find a criterion where contractility sets in. We will assume that we are well into the nematic phase and that the actin density dependence of the myosin on rate has saturated.

We will assume an isotropic groundstate of the following form

$$\rho_m = \rho_m^{(0)} + \delta \rho_m = k^{-1} + \delta \rho_m \quad (\text{S73})$$

$$\rho_a = \rho_a^{(0)} + \delta \rho_a \quad (\text{S74})$$

$$P^i \vec{e}_i = \cos \phi \hat{e}_x + \sin \phi \hat{e}_y = \vec{e}_x + \delta \phi \hat{e}_y \quad (\text{S75})$$

where we have perturbed the  $\phi = 0$  orientation (i.e. all filaments pointing in the  $x$  direction).

At lowest order the molecular field is given by

$$h^i = \Delta P^i, \quad (\text{S76})$$

where  $\Delta$  is the Laplacian. We write the contractility as

$$\zeta = \zeta^{(0)} + \zeta^{(1)} \delta \rho_m \quad (\text{S77})$$

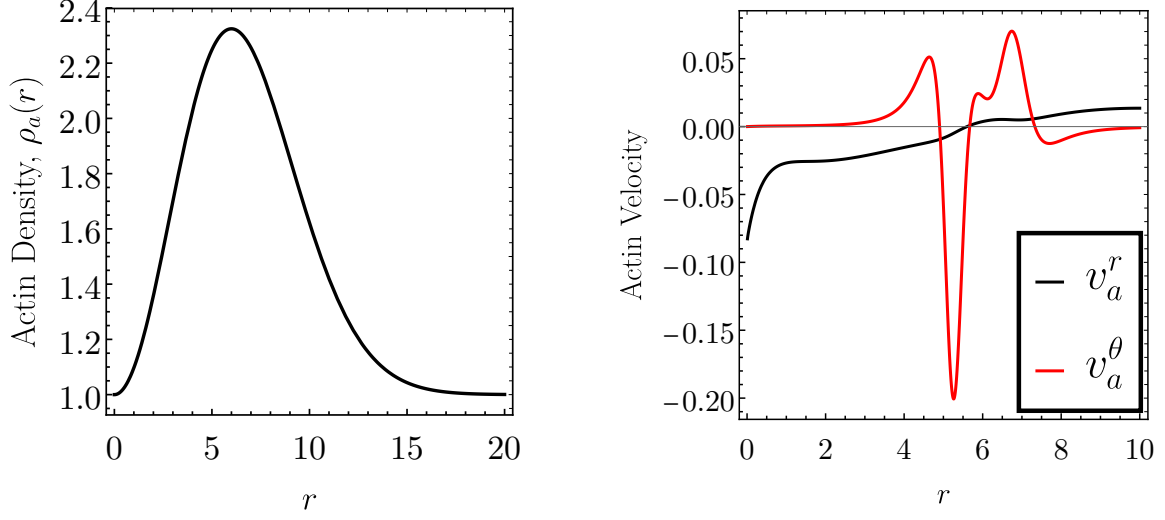


FIG. S14. Figure plotting initial actin density and the first order velocity field for the spiral texture. Plotted for  $\chi_m = 1$ ,  $\chi_a = 0.1$ ,  $R = 6$ ,  $a = 6$ ,  $\kappa = 0.1$ ,  $\xi = -1$  and  $k = 10$ .

The dynamical equations then read

$$\delta\rho_{m,t} = \frac{\chi_a\rho_m^{(0)}}{\rho_a^{(0)}}\nabla^2\delta\rho_a + \left(\frac{\zeta^{(1)}\rho_m^{(0)}}{\rho_a^{(0)}} + \chi_m\right)\nabla^2\delta\rho_m - k\delta\rho_m + \delta\rho_{m,x} + \rho_m^{(0)}\delta\phi_{,y} \quad (\text{S78})$$

$$\delta\rho_{a,t} = \chi_a\nabla^2\delta\rho_a + \zeta^{(1)}\nabla^2\delta\rho_m \quad (\text{S79})$$

$$\delta\phi_{,t} + \frac{\kappa}{4\rho_a^{(0)}}\Delta^2\delta\phi = \kappa\Delta\delta\phi \quad (\text{S80})$$

Fourier transforming in space  $\bar{f}(q) = \int d^2x f(x) \exp(-i\vec{q} \cdot \vec{x})$  where  $\vec{q} = (q_x, q_y)$  and  $\vec{x} = (x, y)$ , we find the following

$$\vec{X}_{,t} = A \cdot \vec{X} \quad (\text{S81})$$

where  $\vec{X} = (\delta\bar{\rho}_m, \delta\bar{\rho}_a, \delta\bar{\phi})^T$  and

$$A = \begin{pmatrix} -\frac{\zeta^{(1)}}{k\rho_a^{(0)}}|\vec{q}|^2 - \chi_m|\vec{q}|^2 + iq_x - k & -\frac{\chi_a}{k\rho_a^{(0)}}|\vec{q}|^2 & i\frac{q_y}{k} \\ -\zeta^{(1)}|\vec{q}|^2 & -\chi_a|\vec{q}|^2 & 0 \\ 0 & 0 & -\frac{|\vec{q}|^2(|\vec{q}|^2 + 4\rho_a^{(0)})}{4\rho_a^{(0)}} \end{pmatrix} \quad (\text{S82})$$

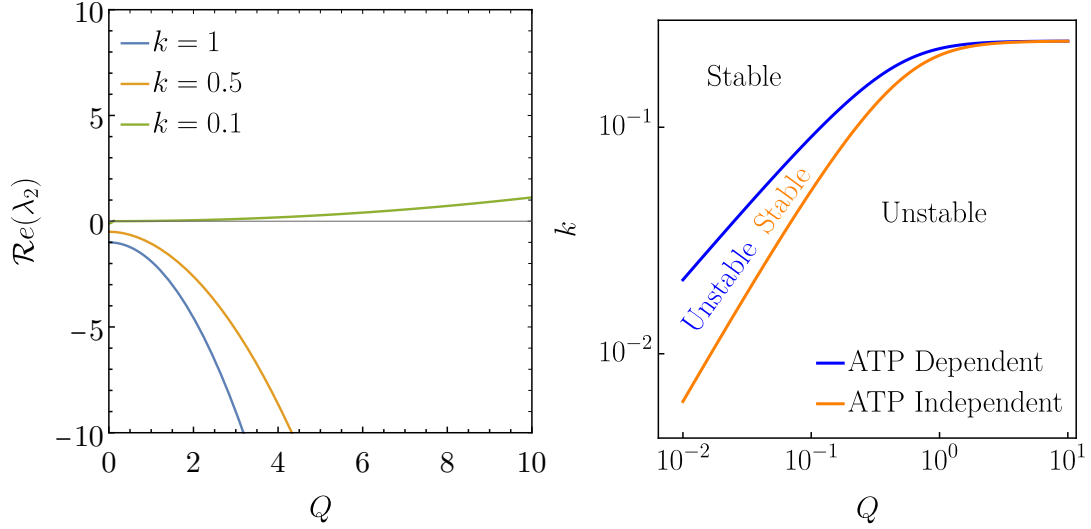


FIG. S15. **Left:** Real part of the second eigenvalue for  $\xi = -1$ ,  $\rho_a^{(0)} = 10$  and  $\chi_m = 1$  for a selection of  $k$  values. **Right:** Stability diagram as a function of  $k$  and  $Q$  for the ATP dependent model (blue) and ATP independent model (orange). The values of  $\xi = -1$ ,  $\rho_a(0) = 10$  and  $\chi_m = 1$  are used here.

We find the following eigenvalues for  $A$

$$\lambda_1 = -\frac{|\vec{q}|^2 \left( |\vec{q}|^2 + 4\rho_a^{(0)} \right)}{4\rho_a^{(0)}}, \quad (\text{S83})$$

$$\lambda_2 = + \frac{\sqrt{\left( \left( \zeta^{(1)} \rho_m^{(0)} |\vec{q}|^2 + \rho_a^{(0)} (|\vec{q}|^2 (\chi_a + \chi_m) - iq_x + k) \right)^2 - 4(\rho_a^{(0)})^2 \chi_a |\vec{q}|^2 (\chi_m |\vec{q}|^2 - iq_x + k) \right)}}{2\rho_a^{(0)}} - \frac{\zeta^{(1)} |\vec{q}|^2 \rho_m^{(0)}}{2\rho_a^{(0)}} + (|\vec{q}|^2 (\chi_a + \chi_m) - iq_x + k), \quad (\text{S84})$$

$$\lambda_3 = + \frac{\sqrt{\left( \left( \zeta^{(1)} \rho_m^{(0)} |\vec{q}|^2 + \rho_a^{(0)} (|\vec{q}|^2 (\chi_a + \chi_m) - iq_x + k) \right)^2 - 4(\rho_a^{(0)})^2 \chi_a |\vec{q}|^2 (\chi_m |\vec{q}|^2 - iq_x + k) \right)}}{2\rho_a^{(0)}} - \frac{\zeta^{(1)} |\vec{q}|^2 \rho_m^{(0)}}{2\rho_a^{(0)}} - (|\vec{q}|^2 (\chi_a + \chi_m) - iq_x + k). \quad (\text{S85})$$

In the low  $q$  limit we find

$$\{\lambda_1, \lambda_2, \lambda_3\} = \left\{ -|\vec{q}|^2, -k + iq_x - \left( \frac{\zeta^{(1)} \rho_m^{(0)}}{\rho_a^{(0)}} + \chi_m \right) |\vec{q}|^2, -\chi_a |\vec{q}|^2 \right\} + O(|q|^3), \quad (\text{S86})$$

where writing  $|q| = Q$ ,  $\rho_m^{(0)} = k^{-1}$  and  $\zeta^{(1)} = \frac{\xi}{k}$  allows us to find the following instability condition for  $\lambda_2$

$$0 \leq -k - \left( \frac{\xi}{k^2 \rho_a^{(0)}} + \chi_m \right) Q^2. \quad (\text{S87})$$

We plot the full growth rate of  $\lambda_2$  in Fig. S15 along with a phase diagram comparing to the case where  $\zeta^{(1)} = \text{Const}$  (where the constant is chosen to match the phase diagram in the high  $Q$  regime).

## 7. Full Numerical Solutions

To solve the full hydrodynamic equations numerically we use a  $100 \times 100$  grid with  $\Delta x = 0.1$  and use a central difference stencil in space. To integrate in time we use a 4<sup>th</sup> order Runge-Kutta method with  $\Delta t = 0.005$  such that the numerical integration is stable (assuming a standard von-Neumann numerical stability condition for reaction diffusion equations). We use bespoke code in C++ to solve this numerically and use PyPlot to create the figures and videos using a script based on openCV functions. We choose a uniform density initial condition on actin  $\rho_a(0) = 10$ , myosin  $\rho_m(0) = 1/k$  and a uniform random orientation on the initial polarisation  $\vec{P} = \cos(\theta)\vec{e}_x + \sin(\theta)\vec{e}_y$  where  $\theta \sim \mathcal{U}[0, 2\pi)$ .